Material point method modeling of granular flow considering phase transition from solid-like to fluid-like states

Hang FENG, Ph.D. Student

State Key Laboratory of Hydroscience and Engineering, Department of Hydraulic Engineering, Tsinghua University, Beijing 100084, China

Department of Civil and Environmental Engineering, The Hong Kong Polytechnic University, Hung Hom, Kowloon, Hong Kong

Weijian LIANG, Research Assistant Professor

(Corresponding author, weijian.liang@polyu.edu.hk)

Department of Civil and Environmental Engineering, The Hong Kong Polytechnic University, Hung Hom, Kowloon, Hong Kong

Zhen-Yu YIN, Professor

(Corresponding author, zhenyu.yin@polyu.edu.hk)

Department of Civil and Environmental Engineering, The Hong Kong Polytechnic University, Hung Hom, Kowloon, Hong Kong

Liming HU, Professor

State Key Laboratory of Hydroscience and Engineering, Department of Hydraulic Engineering, Tsinghua University, Beijing 100084, China

To be submitted to

International Journal for Numerical and Analytical Methods in Geomechanics, Wiley

December 22, 2025

Highlights

- A solid- to fluid-like phase transition model is proposed and implemented in MPM
- The model integrates elastoplasticity for friction stress and kinetic theory for collision stress
- The evolution of state variable granular temperature governs phase transition
- Comparisons with experiment results validate the accuracy of the model
- The model accurately captures solid and fluid states of large deformation granular flow

Abstract

Granular flow is ubiquitous in various engineering scenarios, such as landslides, avalanches, and industrial processes. Reliable modeling of granular flow is crucial for mitigating potential hazards and optimizing process efficiency. However, the complex behavior of granular media, which transitions between solid-like and fluid-like states, poses a significant challenge in their modeling, particularly when involving rapid mobilization. To address this challenge, we propose an innovative constitutive model capable of capturing the highly nonlinear behavior of granular flow by integrating frictional and collisional mechanisms under varying states. The proposed model incorporates two distinct stress components: frictional stress and collisional stress. The frictional stress is governed by a critical-state-based elastoplasticity model, which accurately describes the solid-like behavior of granular media. On the other hand, the collisional stress is formulated using a well-established kinetic theory, which effectively captures the fluid-like behavior of granular media. To seamlessly transition between these two states, we introduce a novel state variable, the granular temperature, which serves as a measure of the kinetic energy of the granular system. This innovative transition model is further incorporated into a GPU-based Material Point Method (MPM) and used to model two types of granular flows, including column collapse and flume tests on an inclined surface. The numerical results show good agreement with available experimental data, highlighting the efficacy of our proposed phase transition model with the MPM modeling approach in effectively capturing the transition of granular materials from solid-like to fluid-like states throughout the mobilization process, from initiation to final deposition.

Keywords: Granular flow; Material point method; Constitutive model; Large deformation modeling; Frictional stress; Collisional stress

1 Introduction

Granular flow phenomena, which are closely associated with natural disasters such as flow-like landslides and debris flows, pose significant threats to both lives and economies (Bocquet et al., 2002; Cascini et al., 2016; Si et al., 2018; Ng et al., 2020; Vicari et al., 2022; Ng et al., 2023; Di Carluccio et al., 2024). These events often initiate as solid-like material that gradually transitions into a fluid-like state, traveling at high velocities. Therefore, accurate assessment of the flowing mass, velocity, and run-out distance of the granular flow is of paramount importance. However, achieving such accurate evaluations necessitates the development of a rational numerical approach coupled with an appropriate constitutive model for granular material. Despite considerable advancements in modeling granular flow, several challenges persist (Cuomo et al., 2019; Augarde et al., 2021; Vicari et al., 2022; Di Carluccio et al., 2024). These include the limitations of numerical procedures in dynamic, large deformation situations, and the need for a rational description of the initiation and propagation mechanisms of granular flow. Particularly challenging is the need to model the transitional behavior of mobilized particles as they shift between solid-like and fluid-like states.

In the literature, a wide range of numerical approaches have been employed for resolving granular flow involving large deformation. Eulerian approaches in Computational Fluid Dynamics (CFD), such as the Finite Volume Method (FVM) (e.g., Yavari-Ramshe et al., 2015; Lin and Yang, 2020; Faroux et al., 2022), Finite Difference Method (FDM) (e.g., Hayat et al., 2021; Haeri and Skonieczny, 2022), and Finite Element Method (FEM) (e.g., Zheng et al., 2015(a), 2015(b); Bai et al., 2017) are notably pervasive. Despite this, these approaches struggle to accurately track particles and interfaces between different materials. Lagrangian-based numerical methods, on the other hand, provide a robust framework for tracking both the interface and material particles with a higher accuracy. Within this framework, a variety of methods have been deployed to tackle large deformation granular flow, including Material Point Method (MPM) (Dunatunga and Kamrin, 2015; Ceccato and Simonini, 2016; Liang and Zhao, 2019; Redaelli et al., 2017; Lei et al., 2022; Liang et al., 2023; Liang et al., 2024), Particle Finite Element Method (PFEM) (Cante et al., 2014; Cremonesi et al., 2020; Larsson et al., 2021; Zhang et al., 2023), and Smoothed Particle Hydrodynamics (SPH) (Guo et al., 2016; Peng et al., 2016; Guo et al., 2020). Among them, MPM stands out as an effective hybrid Eulerian-Lagrangian approach, showing a superior balance

between computational efficiency and accuracy in solving large deformation problems and tracking particle movements. Considering these merits, we have chosen MPM as the numerical tool for our study.

Following the selection of the numerical tool, it is crucial to employ a rational constitutive model to accurately depict the behavior of the granular material during both the inception and propagation stages of flow. In these stages, the granular material manifests different behaviors according to its state. As depicted in Fig.1, granular materials initially exhibit solid-like characteristics before the initiation stage. They then evolve into a fluid-like state with significant velocity during the propagation stage and finally deposit as a solid-like material. This transitional behavior underscores the need for a versatile constitutive model capable of representing the complex dynamics of granular material across various stages.

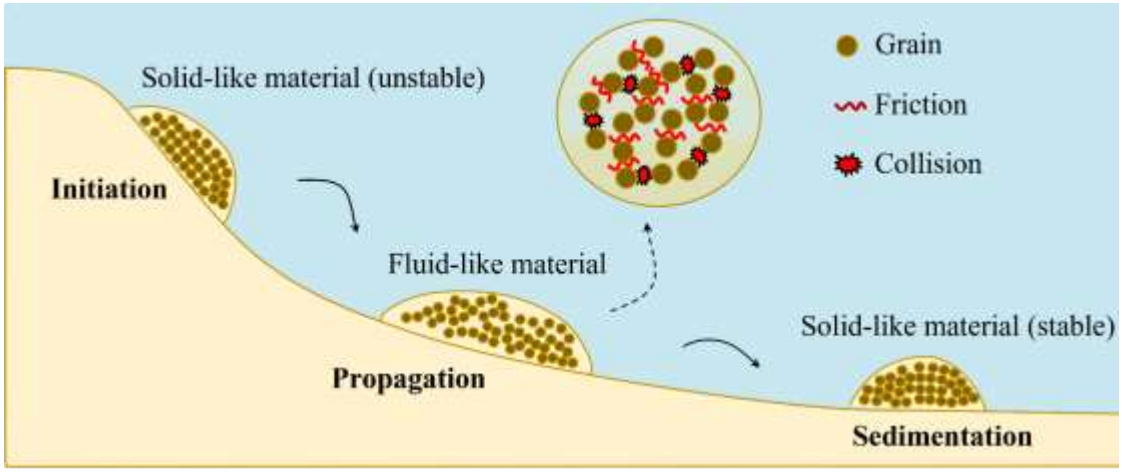

Fig 1. Illustration of different stages in granular flow

The existing models for granular flow can be broadly classified into two categories: soil mechanics-based models and fluid dynamics-based models. The former based on the theory of soil mechanics employs a rate-independent stress to describe granular behavior, which may include hardening or softening, dilatancy, and state-dependence. These models treat the granular material as a solid-like state and thus can effectively predict the initiation of granular flow (Chang and Yin, 2010; Fern and Soga, 2016; Yin et al., 2016; Song et al., 2021; Feng et al., 2024; Wang and Wu, 2024; Zhu et al., 2024). On the other hand, the fluid dynamics-based models employ a rate-dependent rheological law to investigate the propagation of granular flow. These models effectively depict the post-failure behavior of the fluid-like granular material but often fall short of accurately reproducing the pre-failure behavior of the granular media (Pastor et al., 2009; Huang

et al., 2011; Lagrée et al., 2011; Cascini et al., 2014; Dai et al., 2014; Hurley and Andrade, 2017; Franci and Cremonesi, 2019). In this regard, neither the soil mechanics-based nor fluid mechanics-based models can effectively depict the whole process in granular flow including initiation and propagation mobilization stages.

To bridge these gaps, the mentioned two models can be combined to separate the initiation and propagation stages, i.e., the soil mechanics-based model is only used to depict solid-like behavior and the fluid mechanics-based model to depict fluid-like behavior (Pastor et al., 2009; Prime et al., 2014; Dunatunga and Kamrin, 2015). Note that this philosophy requires a rigorous consideration of the interaction between solids and fluids (Peng et al., 2016). To circumvent this complexity, a unified modeling idea that captures both solid-like and fluid-like behavior of the granular flow has been proposed (Vescovi et al., 2013; Redaelli et al., 2015; Peng et al., 2016; Si et al., 2018; Guo et al., 2020; Vescovi et al., 2020; Wang and Wu, 2024). Models based on this idea assume a parallel scheme in which the stress is calculated as the sum of frictional and collisional contributions (see Eq.(1)) (Johnson and Jackson, 1987; Johnson et al., 1990; Savage, 1998; Louge, 2003; Lee and Huang, 2010; Vescovi et al, 2013; Redaelli et al, 2015; Si et al., 2018). The former is associated with long elapsing frictional contacts while the latter with collisional mechanisms (see Fig.1).

$$\boldsymbol{\sigma} = \boldsymbol{\sigma}_f + \boldsymbol{\sigma}_{col} \tag{1}$$

where $\boldsymbol{\sigma}$ is the Cauchy stress tensor, $\boldsymbol{\sigma}_f$ is the quasi-static stress; $\boldsymbol{\sigma}_{col}$ is the collisional stress.

Recently, a few phase transition models based on the parallel scheme have been proposed (e.g., Vescovi et al., 2013; Redaelli et al., 2015; Si et al., 2018; Guo et al., 2016; Peng et al., 2016; Guo et al., 2020; Wang and Wu, 2024); however, an effective model remains under investigation. To the authors' knowledge, existing solid-like stress components in phase transition models primarily adopt simplified granular materials, neglecting key characteristics such as hardening or softening, dilatancy, and state-dependent characteristics, particularly the critical state that triggers the fluid-like behavior (e.g., Vescovi et al., 2013; Redaelli et al., 2015; Si et al., 2018). Consequently, we have proposed a straightforward yet effective critical-state-based elastoplastic stress model that incorporates these essential characteristics, thereby enhancing the complicated behavior of frictional mechanisms during granular flow.

Another significant aspect of phase transition models is the fluid-like stress representation. Existing models can be categorized into two types according to the expression of fluid-like stress: those employing phenomenological Non-Newtonian viscous models, such as the μ(I) constitutive relationship (Jop et al., 2006; Wang and Wu, 2024), and those grounded in kinetic theory related to particle collisional mechanisms (e.g., Vescovi et al., 2013; Si et al., 2018; Vescovi et al., 2020; Redaelli et al., 2017). Both approaches effectively capture the viscous properties in fluid-like states. Our study proposes a solid-fluid phase transition model that incorporates the μ(I) constitutive relationship. However, it remains unclear whether the combination of the proposed critical-state-based elastoplastic stress model with kinetic theory can effectively represent the solid-fluid phase transition. To address this issue, we propose a novel phase transition constitutive model incorporating the kinetic theory. This model integrates the critical-state-based elastoplasticity framework to depict the frictional contribution in the solid-like state, and a kinetic theory to describe the collisional contribution in the fluid-like state. An intrinsic state variable granular temperature is introduced to control the phase transition between these states.

This work aims to solve the large deformation granular flow using MPM with the novel phase transition constitutive model that can depict the behavior of granular material from a solid-like to a fluid-like state during the initiation and propagation stage. The paper is organized as follows: Section. 2 presents governing equations and numerical procedure of the material point method in granular flow. Section 3 elaborates on the phase transition constitutive model and its element test simulation. The numerical examples of this constitutive model are presented in Section. 4. The major conclusions are drawn in Section. 5.

2 Material point method

2.1 Governing equations

In MPM, the mass and momentum conservation equations for the continuum material take the following expression:

$$\dot{\rho} = -\rho \nabla \cdot \mathbf{v} \tag{2}$$

$$\rho \dot{\mathbf{v}} = \nabla \cdot \boldsymbol{\sigma} + \mathbf{b} \tag{3}$$

where ρ is the density; $\dot{\rho}$ denotes the material time derivative of the density; $\mathbf{v}$ is the velocity; $\dot{\mathbf{v}}$ denotes the material time derivative of the velocity; $\boldsymbol{\sigma}$ is the Cauchy stress tensor; **b** is the body force per unit volume.

Multiplying Eq. (3) by an arbitrary virtual vector-valued displacement function $\delta\mathbf{u}$, the weak form of the momentum equation is expressed as:

$$\int_{\Omega} \rho \dot{\mathbf{v}} \cdot \delta \mathbf{u} \, d\Omega = -\int_{\Omega} \boldsymbol{\sigma} : \nabla \delta \mathbf{u} \, d\Omega + \int_{\Omega} \mathbf{b} \cdot \delta \mathbf{u} \, d\Omega + \int_{\Gamma} \mathbf{t} \cdot \delta \mathbf{u} \, d\Gamma \tag{4}$$

where Ω represents the material domain; Γ denotes the boundary and **t** is the surface traction.

2.2 GPU-based MPM

In MPM, two descriptions are adopted for the targeted continuum media, namely Eulerian (i.e., stationary background grid) and Lagrangian (i.e., material points) descriptions. The Lagrangian material points are employed to store the material information (e.g., the velocity, displacement, stress, and strain). The Eulerian gird is adopted to solve the governing equation. The grid information will be reset at the beginning of each step. The information transforms between the Lagrangian material particles and Eulerian grids via the shape function.

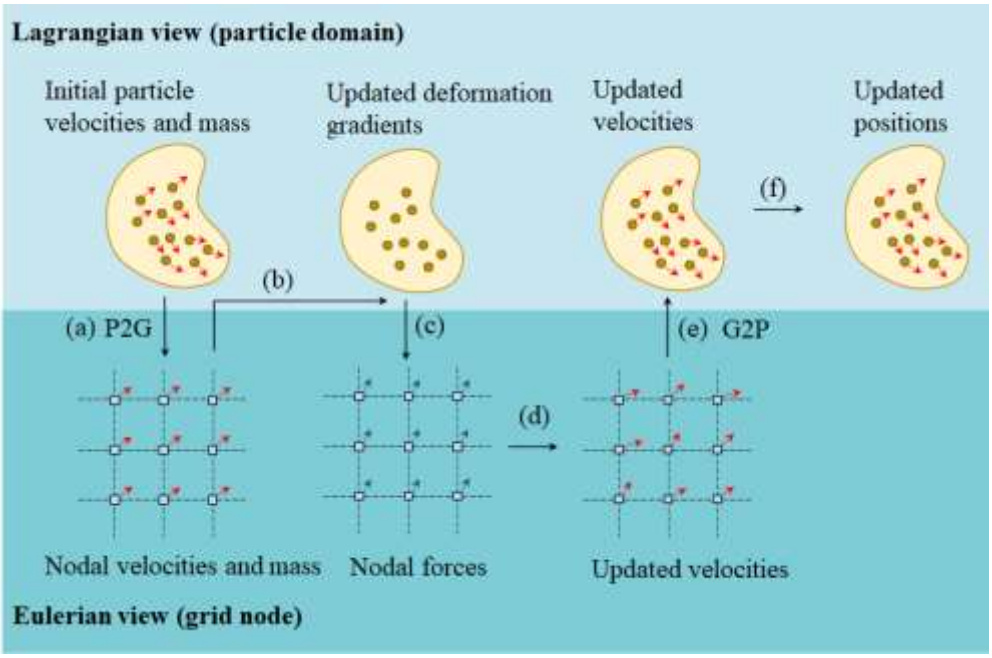

Fig. 2. Illustration of the material point method computational procedure

To solve Eq. (4), the material domain is discretized into a set of material points that travel over the fixed computational grid. The information of particles can be approximated using the information of the grid node. As shown in Fig. 2, the typical MPM computation procedure includes the following main steps:

(a) Particle to Grid (i.e., P2G): At the current step t^k, the information of particles (i.e., particle mass m_p and velocity $\mathbf{v}_p^k$) is interpolated to the background grid node via the shape function $N_{Ip}^k = N_I(\mathbf{x}_p^k)$. Subsequently, the nodal mass m_I^k and nodal velocity $\mathbf{v}_I^k$ are obtained using Eqs. (5) and (6):

$$m_I^k = \sum_p N_{Ip}^k m_p \tag{5}$$

$$\mathbf{v}_I^k = \left(\sum_p N_{Ip}^k m_p \mathbf{v}_p^k \right) \Big/ m_I^k \tag{6}$$

(b) Updating particle deformation gradients: Compute velocity gradient $\nabla \mathbf{v}_p^k$ and deformation gradient $\boldsymbol{F}$ of the particles by the nodal velocity $\mathbf{v}_I^k$:

$$\nabla \mathbf{v}_p^k = \sum_I \nabla N_{Ip}^k \, \mathbf{v}_I^k \tag{7}$$

$$\mathbf{F}_p^k = \left(1 + \nabla \mathbf{v}_p^k \Delta t\right) \mathbf{F}_p^{k-1} \tag{8}$$

(c) Updating nodal forces: Using the particle deformation gradient $\mathbf{F}_p^k$, the particle strain can be updated via Eq.(9). With this strain $\boldsymbol{\varepsilon}^k$, an appropriate constitutive model is then employed to calculate the stress $\boldsymbol{\sigma}^k$, which will be discussed in Section. 3. Then, the internal force $\mathbf{f}_I^{int,k}$ is calculated via $\mathbf{f}_I^{int,k} = -\sum_p \boldsymbol{\sigma}_p^k \cdot \nabla N_{Ip}^k V_p^k$. The external force $\mathbf{f}_I^{ext,k}$ only considers the gravity in the typical granular flow.

$$\boldsymbol{\varepsilon}^k = \frac{1}{2}\left(\mathbf{F}_p^k + \left(\mathbf{F}_p^k\right)^T\right) - \mathrm{I} \tag{9}$$

(d) Updating nodal velocities: The nodal acceleration and velocity can be updated using $\mathbf{a}_I^k = (\mathbf{f}_I^{int,k} + \mathbf{f}_I^{ext,k}) / m_I^k$ and $\mathbf{v}_I^{k+1} = \mathbf{v}_I^k + \mathbf{a}_I^k \, \Delta t$, respectively.

(e-f) Grid to Particle (G2P): The velocity and position of particles can be interpolated from the grid nodes using Eqs. (10) and (11):

$$\mathbf{v}_p^{k+1} = \mathbf{v}_p^k + \sum_I \mathbf{a}_I^k \, N_{Ip}^k \, \Delta t \tag{10}$$

$$\mathbf{x}_p^{k+1} = \mathbf{x}_p^k + \sum_I \mathbf{v}_I^{k+1} \, N_{Ip}^k \, \Delta t \tag{11}$$

The numerical stages (a~f) constitute a calculation loop designed to update the particle information. For the next step time, the information of the background grid is discarded, and therefore, the grid node position remains unchanged throughout the simulation.

Considering that the MPM modeling requires the solution of a large number of linear equations at each time step, GPU-empowered parallel computing is expected to significantly leverage the overall computational efficiency (Dong et al., 2015; Dong and Grabe, 2018; Wang et al., 2023). In this study, a domain-specific language (DSL) Taichi, is utilized to facilitate high-performance, GPU-based simulation (Hu et al., 2019; He et al., 2024). Taichi is an open-source,

parallel programming language that is embedded within Python. It employs just-in-time (JIT) compiler frameworks to facilitate efficient numerical computation. By using the @ti.kernel decorator, Taichi enables the JIT compiler to automatically compile Python functions into optimized GPU machine code for parallel execution. This feature allows one to achieve GPU acceleration with considerable ease, without requiring extensive knowledge of GPU architectures and programming models. At present, Taichi supports most mainstream GPU APIs, such as CUDA and Vulkan. Accordingly, all the simulations are written in Python with Taichi and employed in CUDA to achieve high-performance MPM modeling.

3 Phase transition model

For granular flow, the material involved exhibits highly nonlinear behavior as it could transition between solid-like and fluid-like states. In this regard, a novel phase transition constitutive model for the granular media is introduced in this section to accurately capture this behavior and complete the MPM framework.

3.1 Basic framework

To propose a constitutive model potent enough to delineate the phase transition from solid-like to fluid-like state, a fundamental assumption for granular flow is adopted (Vescovi et al., 2013; Redaelli et al., 2015; Peng et al., 2016; Si et al., 2018; Guo et al., 2020; Vescovi et al., 2020; Wang and Wu, 2024), which posits that the energy of the granular material system is dissipated by two main mechanisms among particle interactions, namely friction and collision (Jaeger et al., 1996; Ancey, 2007; Chen and Yan, 2021). Based on this assumption, the granular flow can be divided into three regimes:

(i) *Quasi-static regime*: predominated by friction mechanism, the granular material is dense and behaves as a solid. The stress is primarily the friction-induced stress generated by force chains through particle contacts. This friction-induced stress is also referred to as quasi-static stress.

(ii) *Collisional regime*: dominated by collision mechanism, the density of the granular material is low. The granular material is mainly governed by collisional stress.

(iii) *Transitional regime*: this regime occurs when particles interact via both collision and friction mechanisms, with the material exhibiting fluid-like behavior governed by both collision-induced and friction-induced stresses.

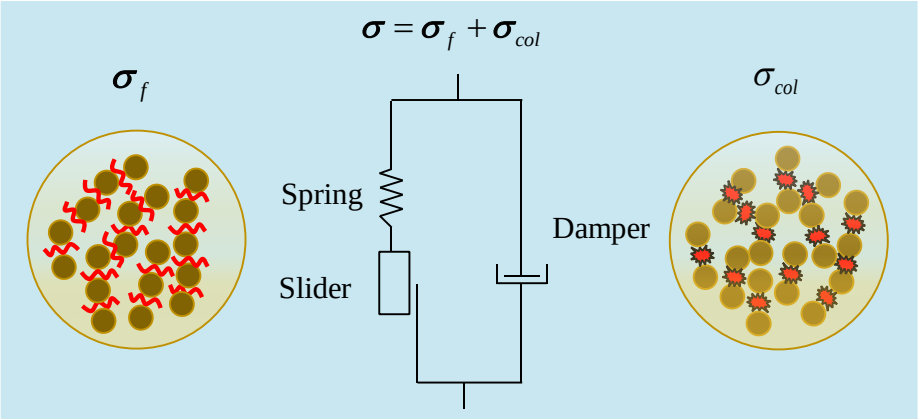

Fig 3. Illustration of the parallel scheme for the phase transition model

Given the aforementioned setup, a theoretical framework known as the parallel scheme has been employed. In this scheme, the total granular stress is decomposed into friction-induced stress and collision-induced stress as indicated in Eq. (1). Fig.3 depicts the parallel scheme for the phase transition constitutive model. The friction-induced stress $\boldsymbol{\sigma}_f$ is strain rate-independent, which can be described using an elastic spring in series with a slider (i.e., the elastoplasticity theory), while the strain rate-dependent collision-induced stress $\boldsymbol{\sigma}_{col}$ is described using a damper. Both types of stress coexist throughout the entire deformation process.

Based on the parallel scheme, we have proposed an innovative constitutive model to depict the phase transition from a solid-like to a fluid-like state, effectively capturing the following behaviors during the transition: (i): the quasi-static stress $\boldsymbol{\sigma}_f$ is depicted via an elastoplasticity framework, which can rationally depict the solid-like state with key characteristics such as nonlinear elasticity, nonlinear plastic hardening, dilatancy, and state-dependent characteristics before the initiation of the granular flow. (ii): the critical state theory (Roscoe et al. 1958; Worth, 1958; Schofield and Wroth, 1968) is incorporated into the elastoplasticity framework to depict the initiation of the granular flow (i.e., the inception of fluid-like material and the failure of the granular solid-like material), where the granular material begins to deform indefinitely without further change in stresses and volume. (iii): the kinetic theory is used to describe the collisional stress in the fluid-like state. By employing granular temperature as a state variable to represent collisional

stress, the entire phase transition of granular flow from solid-like to fluid-like can be rationally and smoothly depicted.

3.2 Frictional stress

In the proposed phase transition model, the frictional stress is expressed via a critical state-based Mohr-Coulomb model. This model employs the framework of an elastoplasticity model SIMSAND (Yin et al., 2013; Yin et al., 2014; Jin et al., 2017; Yin et al., 2020), which has demonstrated a superior capability in reproducing the nonlinear elasticity, nonlinear plastic hardening, stress dilatancy (contraction or dilation), and critical state of granular material. In a similar manner, the frictional contribution is decomposed into an elastic part and a frictional part. Using an incremental form, the strain increment $\delta\boldsymbol{\varepsilon}_{ij}$ is divided into the elastic increment $\delta\boldsymbol{\varepsilon}_{ij}^{e}$ and plastic increment $\delta\boldsymbol{\varepsilon}_{ij}^{p}$:

$$\delta\boldsymbol{\varepsilon}_{ij} = \delta\boldsymbol{\varepsilon}_{ij}^{e} + \delta\boldsymbol{\varepsilon}_{ij}^{p} \tag{12}$$

The elastic strain increment $\delta\boldsymbol{\varepsilon}_{ij}^{e}$ can be employed to obtain the frictional stress increment via $\Delta\boldsymbol{\sigma}_{f} = D_{f} : \Delta\boldsymbol{\varepsilon}_{ij}^{e}$ (in which D_{f} is the elastic stiffness matrix related to the elastic bulk modulus K_{f} and Poisson's ratio *v*). The dependence of elastic bulk modulus on the pressure and void ratio is considered herein (i.e., nonlinear elasticity), which is expressed as follows:

$$K_{f} = K_{0} p_{at} \frac{(2.97-e)^{2}}{(1+e)} \left(\frac{p_{f}}{p_{at}} \right)^{n} \tag{13}$$

where p_{at} is the atmospheric pressure (i.e., p_{at}=101.3 kPa); *n* is the elastic constant controlling nonlinear stiffness; p_{f} is the hydrostatic frictional stress; *e* is the void ratio, its evolution is calculated via $\dot{e} = -(1+e)\mathrm{Tr}(\boldsymbol{\varepsilon})$; K_{0} is the dimensionless referential bulk modulus.

The distinction between elastic and plastic behaviors is determined by the yield criterion. When the stress state lies within the yield surface *f*, the material exhibits elastic behavior. Conversely, when it lies beyond this surface, irreversible plastic behavior ensues. The corresponding plastic strain increment is calculated using the flow rule $\delta\boldsymbol{\varepsilon}_{ij}^{p} = d\lambda \frac{\partial g}{\partial \boldsymbol{\sigma}_{ij}}$ (in which

290 $d\lambda$ is the plastic multiplier; g is the plastic potential function). The associated flow rule is
291 considered herein (i.e., the plastic potential function coincides with the yield surface). It's important
292 to note that the consistency law $\dot{f} = 0$, which indicates the stress state remains on the yield surface
293 after yielding, is essential for calculating the plastic multiplier.

294 To accurately represent the frictional yielding characteristic, we employ the widely
295 recognized Mohr-Coulomb yield criterion, commonly used for granular materials in the
296 geotechnical field. This criterion incorporates the frictional asymptotic strength characteristic of
297 sands, an aspect often referred to as nonlinear plastic hardening. This can be expressed as follows:

298 $$f = \frac{q_f}{p_f} - \frac{M\varepsilon_d^p}{k_p + \varepsilon_d^p} \tag{14}$$

299 where q_f is the deviatoric frictional stress; M is the slope of the failure line in the p_f-q_f plane, which
300 is expressed as $M_p = 6\sin\phi_c / (3 - \sin\phi_c)$.

301 To facilitate the consideration of the stress dilatancy (contraction or dilation), the plastic
302 potential function is expressed as follows:

303 $$\frac{\partial g}{\partial p_f} = A_d\left(M_{pt} - \frac{q_f}{p_f}\right), \frac{\partial g}{\partial q_f} = 1 \tag{15}$$

304 where A_d is a parameter controlling the magnitude of the stress-dilatancy; M_{pt} is the transformation
305 stress ratio which corresponds to the transitional state between a contractive behavior under low
306 stress ratios and a dilatancy behavior under higher stress ratios. If the current stress ratio is smaller
307 than M_{pt}, the material is contractive. Otherwise, it is dilative.

308 Based on the critical state theory, the critical void ratio e_c is considered as below:

309 $$e_c = e_{\text{ref}} \exp\left[-\lambda\left(\frac{p_f}{p_{at}}\right)^{\xi}\right] \tag{16}$$

310 where e_{ref} is a reference void ratio; λ is the slope of the critical state line (CSL) in the e-logp_f plane;
311 parameter ξ controls the nonlinearity of the critical state line.

The effect of void ratio on the stress-strain-chelaship is implemented by modifying the peak strength ratio with $M_p = 6\sin\phi_p / \left(3-\sin\phi_p\right)$ and the phase transformation stress ratio with $M_{pt} = 6\sin\phi_{pt} / \left(3-\sin\phi_{pt}\right)$. The peak friction angle ϕ_p and transformation angle ϕ_{pt} are expressed as:

$$\phi_p = \arctan\left[\left(\frac{e_c}{e}\right)^{n_p} \tan\phi_c\right] \tag{17}$$

$$\phi_{pt} = \arctan\left[\left(\frac{e}{e_c}\right)^{n_d} \tan\phi_c\right] \tag{18}$$

where n_p and n_d are parameters controlling the effect of particle interlocking. When the granular material is dense (i.e., $e<e_c$), the ϕ_{pt} is initially smaller than ϕ_c, representing a dense structure that is initially contractive and then dilative. When the material is loose (i.e., $e>e_c$), the ϕ_{pt} is larger than ϕ_c, which leads to a contractive behavior. Both loose and dense sands will arrive at a critical state, resulting in the initiation of the granular flow.

In summary, the frictional stress contribution adopts the critical state-based nonlinear Mohr-Coulomb model following the framework of SIMSAND. The nonlinear elasticity, nonlinear plastic hardening, and stress dilatancy are expressed using Eq. (13)-(15), respectively. The critical state theory depicting the initiation of the granular flow is mainly expressed by Eqs. (16)-(18). The effectiveness of this elastoplasticity has been verified in (Yin et al., 2013; Yin et al., 2014; Jin et al., 2017; Yin et al., 2020).

3.3 Collisional stress

When the granular material enters the collisional regime, it exhibits a fluid-like state, and the interactions among particles mainly occur through collisional contacts. Within this collisional regime, the Cauchy stress is mainly governed by the collisional component, which can be determined via the well-established kinetic theory (Jenkins and Savage 1983; Garzo and Dufty 1999, Jenkins and Zhang 2002; Jenkins 2006, 2007; Berzi et al., 2011; Vescovi et al., 2013). According to the kinetic theory, the collisional stress, which represents the rheological characteristics, can be expressed as:

$$\boldsymbol{\sigma}_{col} = \boldsymbol{p}_{col}\delta_{ij} - 2\eta\left(\dot{\boldsymbol{\varepsilon}}_{ij} - \frac{1}{3}\delta_{ij}\nabla\cdot\mathbf{u}\right) - \gamma\left(\nabla\cdot\mathbf{u}\right)\delta_{ij} \tag{19}$$

where $\boldsymbol{p}_{col}$ is the collisional hydrostatic pressure; η is the shear viscosity quantifying the resistance to shear flow; γ is the bulk viscosity measuring the resistance to compression or expansion; $\dot{\boldsymbol{\varepsilon}}_{ij}$ is the strain rate tensor, which is defined as $\dot{\boldsymbol{\varepsilon}}_{ij} = \left(\nabla\mathbf{u} + \nabla^T\mathbf{u}\right)/2$.

It has been clearly shown in previous studies that the collisional pressure $\boldsymbol{p}_{col}$, the shear viscosity η, and the bulk viscosity γ are generally expressed as (Jenkins and Savage, 1983):

$$\boldsymbol{p}_{col} = 4G\left(e\right)F\left(e,\varepsilon_n\right)\rho T \tag{20}$$

$$\eta = \frac{8}{5\sqrt{\pi}}G\left(e\right)J\left(e,\varepsilon_n\right)\rho dT^{0.5} \tag{21}$$

$$\gamma = \frac{4}{3\sqrt{\pi}}G\left(e\right)Q\left(e,\varepsilon_n\right)\rho dT^{0.5} \tag{22}$$

$$G\left(e\right) = V_s g_0\left(V_s\right) = \frac{\rho_p}{1+e}g_0\left(V_s\right) \tag{23}$$

where *d* is the diameter; ρ is the density of the granular medium, which can be computed via $\rho = V_s\rho_p = \rho_p/\left(1+e\right)$ (in which ρ_p denotes the particle density, usually takes 2.65 g/cm³ for the sands; V_s is the volume fraction calculated via $V_s = 1/\left(1+e\right)$); *T* is the granular temperature; *F*, *J*, and *Q* are the auxiliary functions (refer to Appendix A). These functions are related to the void ratio *e* and coefficient of restitution ε_n (i.e., a parameter depicting the restitution during the collision), which is further modified to consider the effect of the tangential contact during the collision. Based on the numerical results using the discrete element method (DEM), Chialvo and Sundaresan (2013) proposed that ε_n should be replaced by the effective coefficient ε_r, as follows:

$$\varepsilon_r = \varepsilon_n - \frac{3}{2}\mu_p\exp\left(-3\mu_p\right) \tag{24}$$

in which μ_p is the friction coefficient, typically takes the value 0-0.5, $g_0\left(V_s\right)$ is the radial distribution function depending on the volume fraction V_s, expressed in Eq. (25):

$$g_0(e) = f(e)\frac{2-V_s}{2(1-V_s)^3} + (1-f(e))\frac{2}{V_{sd}-V_s} \tag{25}$$

$$f(e) = \begin{cases} 1 & \text{if } (V_s < V_m) \\ \dfrac{V_s^2 - 2V_m V_s + V_{sd}(2V_m - V_{sd})}{2V_{sd}V_m - V_m^2 - V_{sd}^2} & \text{otherwise} \end{cases} \tag{26}$$

where V_{sd} represents the densest possible disordered configuration of the granular material, can be determined using the void ratio parameter e_{sd} of the granular material (i.e., $V_{sd} = 1/(1+e_{sd})$); V_m is a function parameter, taken as 0.4.

Eqs. (21)-(24) indicates that the evolution of the collisional pressure $\boldsymbol{p}_{col}$, the shear viscosity η, and the bulk viscosity γ depends on the state variable granular temperature *T*. It is clear that the collisional stress increases with the rising of the granular temperature *T*. Accordingly, evaluating this state variables is substantial, which can be determined using the fluctuating energy balance, as expressed (detailed expressions are provided in Appendix B):

$$\boldsymbol{\sigma}_{\mathrm{col}} : \dot{\boldsymbol{\varepsilon}} = \frac{3}{2}\frac{\rho_p}{1+e}\dot{T} + \nabla \cdot \mathbf{q}_{col}^{E} + \Gamma_{col} \tag{27}$$

The first term on the right of Eq. (29) describes the work by the collisional stress; the second term on the left is the rate of kinetic fluctuating energy; the third term is the divergence of the flux of energy $\mathbf{q}_{col}^{E}$. For the sake of simplicity, the energy flux is not considered following (Berzi et al., 2011; Vescovi et al., 2013); the fourth term Γ_{col} is the energy dissipated by the collisional mechanism, which is expressed as:

$$\Gamma = \frac{144}{5\sqrt{\pi}}\frac{\rho}{d}\frac{T^{3/2}\zeta^*}{(1+e)} \tag{28}$$

where ζ^* is reported in Appendix B.

To sum up, the collisional stress contribution adopts the kinetic theory. The evolution of stress is expressed using Eqs. (19)-(26). The evolution of key state variable granular temperature is expressed using Eqs. (27)-(28). The effectiveness of this collisional stress model has been verified by (Jenkins and Zhang, 2002; Jenkins 2006, 2007; Berzi et al., 2011; Vescovi et al., 2013).

3.4 Element test simulation

Before conducting practical simulations of granular flow, it is essential to evaluate the performance of the proposed phase transition model. This subsection initially examines the behavior of the frictional stress in the small strain rate range and the collisional stresses in the high strain rate regime, followed by an assessment of the unified model's capacity to describe the phase transition.

3.4.1 Simulation of frictional stress

As previously discussed, the frictional stress component in such a model must accurately represent the frictional behavior both before the initiation of flow and at the critical state—where granular flow is triggered. Herein, we select the undrained simple shear tests (during which the volume strain remains constant) to evaluate the frictional stress performance (Guo et al., 2016; Peng et al., 2016; Guo et al., 2020; Wang and Wu, 2024). We employ p_f, q_f, and γ to represent the normal fictional stress, shear fictional stress, and shear strain, respectively. The material parameters reported by Yin et al. (2018) are considered to simulate the frictional stress (see Table. 1).

Fig. 4 presents the results for samples with different void ratios (i.e., e_0=0.80, 0.85, 0.90, 0.95). The dense cases (i.e., e_0=0.8, 0.85) show a dilation tendency and shear hardening, reaching the critical state line eventually, while the loose case (i.e., e_0=0.95) displays shear softening characteristics, attaining a relatively low residual strength at the critical state. The specimens with a medium void ratio (i.e., e_0=0.9) first soften, then harden, and finally reach the critical state line. These observations demonstrate that the frictional stress part can rationally depict the frictional characteristic before the initiation and critical state.

Table 1. Material parameters in the frictional stress model

K_0	v	n	φ	e_{ref}	λ	ξ	A_d	k_p	n_p	n_d
150	0.22	0.6	30	0.937	0.022	0.71	4	0.001	1	1

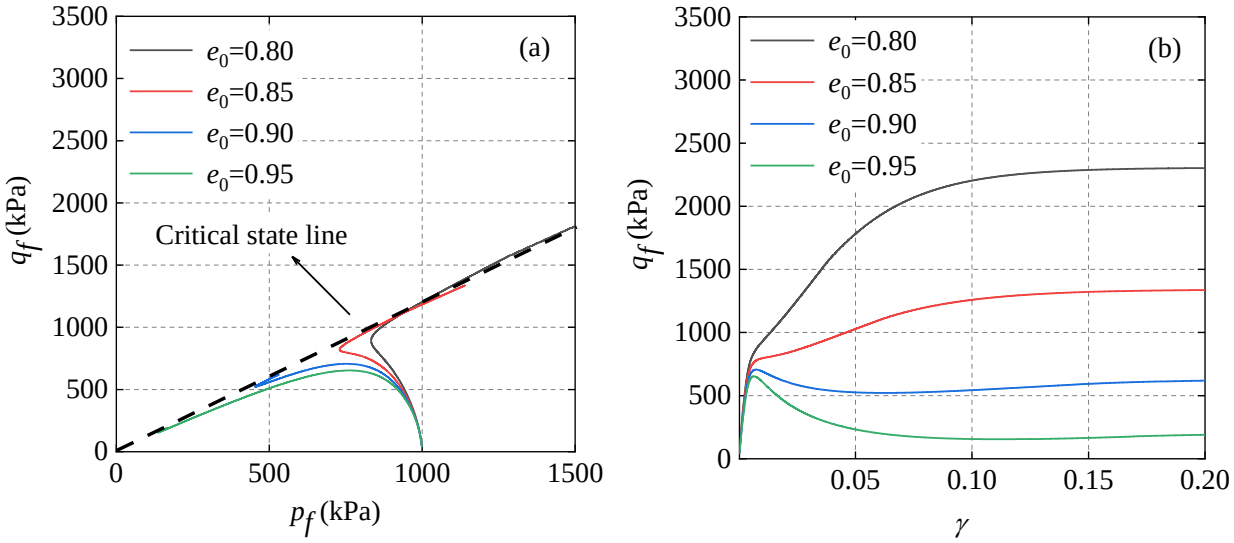

Fig 4. Simulation results for frictional stress with different initial void ratios in undrained simple shear tests: (a) vertical stress versus shear stress; (b) shear strain versus shear stress.

3.4.2 Simulation of collisional stress

Conversely, the collisional stress should rationally express the viscous characteristics when the strain rate is relatively large. Accordingly, this subsection examines the evolution of collisional stress during the large strain rate range via the undrained simple shear test. Both the normal (p_{col}) and shear (q_{col}) collisional stresses under the undrained simple shear test can be deceived based on the equations presented in subsection 3.3. The key parameters for these element test simulations are listed in Table 2. A constant strain acceleration of 50 s^{-2} is applied from 0 s to 3 s, and simulations are conducted across varying initial void ratios (i.e., e_0=0.80, 0.85, 0.90, 0.95).

Table 2. Material parameters in the collisional stress model

ρ_p (kg/m^3)	d (m)	V_{sd}	V_m	ε_n	μ_p
1500	1×10^{-3}	0.6	0.4	0.6	0.2

Fig. 5 presents the simulation results of the undrained simple shear test using the collisional stress model. It is evident that collisional stress rises with increasing strain rates, due to the elevated strain rate enhancing the granular temperature, which in turn amplifies the collisional stress. Similar observations can be obtained from the μ(I) relation proposed by Jop et al. (2008), suggesting that kinetic theory may also serve as a viable alternative model to the μ(I) relation. It also shows that lower initial void ratios yield higher collisional stress values, being consistent with

observations in Section 3.4.1. These findings support the effectiveness of the collisional stress model in capturing viscous behavior under large strain conditions.

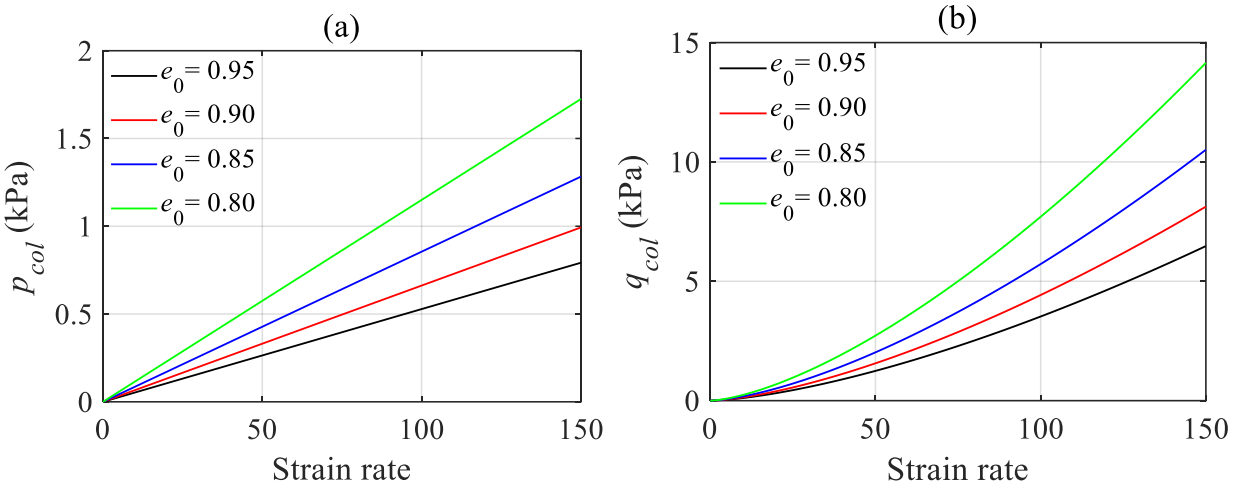

Fig 5. Simulation results for collisional stress with different initial void ratios in undrained simple shear tests: (a) vertical stress versus shear stress; (b) shear strain versus shear stress.

3.4.3 Simulation of phase transition model

The proposed phase transition model combines strain rate-independent frictional stress at small strains with strain rate-dependent collisional stress at large strains via Eqs. (1), (12)-(28). Key characteristics such as nonlinear elasticity, nonlinear plastic hardening, stress dilatancy, and the critical state concept are incorporated into the frictional stress, while the granular temperature is employed to depict the evolution of collisional stress, further capturing its evolution.

Table.3 lists the key parameters in this model. The parameters for the collisional part include: particle density ρ_p and diameter d characterize the particle; friction coefficient μ_p (typically 0 to 0.5) and normal restitution coefficient ε_n (typically 0 to 1) describe the effective collisional contact; void ratio parameter e_{sd} and volume fraction parameter V_m (typically 0.4) are used to depict the radial distribution function. Detailed discussions about these values are provided by Redaelli et al. (2017) and Si et al. (2018). For the frictional stress part, dimensionless referential bulk modulus K_0, Poisson's ratio ν, and Elastic constant controlling nonlinear stiffness n describe the elastic response. Parameters e_{ref}, λ, and ξ illustrate the evolution critical void ratio. Coefficients A_d and k_p characterize the nonlinear plastic hardening. Parameters n_p and n_d depict the stress dilatancy and shear softening. Thorough discussions about the frictional stress parameter can be found in Yin et

al. (2020). Except for the above parameters, state variables including the initial void ratio e_0 and granular temperature T_0 are required in an explicit algorithm.

Table 3. Input parameters in the proposed phase transition model

	Symbol	Parameter	Element test	Column collapse	Flume test
$\boldsymbol{\sigma}_f$	ρ_p	Particle density (kg/m^2)	1050	2650	2500
	d	Diameter (m)	1.0×10^{-3}	1.25×10^{-3}	1.0×10^{-3}
	e_{sd}	Void ratio parameter	0.92	0.62	0.60
	V_m	Volume fraction parameter	0.4	0.4	0.4
	ε_n	Normal restitution coefficient	0.7	0.6	0.6
	μ_p	Friction coefficient	0.1	0.2	0.2
	T_0	Initial granular temperature (10^3 m^2/s^2)	-	$1.0\cdot10^{-15}$	$1.0\cdot10^{-15}$
$\boldsymbol{\sigma}_{col}$	K_0	Dimensionless referential bulk modulus	120	120	130
	v	Poisson's ratio	0.235	0.2	0.2
	p_{at}	Atmospheric pressure (kPa)	101.3	101.3	101.3
	n	Elastic constant controlling nonlinear stiffness	0.5	0.5	0.5
	φ	Critical-state friction angle	23	19.8	38
	e_{ref}	Initial critical-state void ratio	0.910	0.977	0.977
	λ	Parameter controlling the nonlinearity of CSL	0.122	0.0596	0.0596
	ξ	Parameter controlling the nonlinearity of CSL	0.71	0.365	0.365
	A_d	Stress dilatancy constant	0.5	0.7	0.4
	k_p	Plastic modulus-related constant	0.001	0.0044	0.0044
	n_p	Interlocking related peak strength parameter	1	2.4	2.4
	n_d	Interlocking related phase transformation parameter	1	2.9	2.9
	e_0	Initial void ratio	0.99, 1.02,1.05	0.95	0.90

To further evaluate the proposed phase transition model, we conduct an undrained simple shear test simulation and compare the results with the experimental findings of Savage and Sayed (1984). Note that the original experiments employed annular shear tests to examine granular material behavior under constant volume conditions; thus, undrained simple shear tests are suitable

for replicating these conditions (Guo et al., 2016; Wang and Wu, 2024). This study uses polystyrene beads as the test material, with parameters detailed in Table 3. The initial vertical stress is set at 500 Pa, following the parameters from Guo et al. (2016) and Wang and Wu (2024). The simulation begins with a shear rate of 10 s^{-1} and zero strain acceleration for the first 0.5 seconds, followed by a strain rate acceleration of 50 s^{-2} applied from 0.5 to 20 seconds.

Fig. 6 compares the experimental results and numerical solutions for the undrained simple shear test of polystyrene beads. The remarkable agreement of numerical solutions across varying void ratios with experimental data validates the accuracy of the proposed phase transition model. Fig. 7 further illustrates the contributions of vertical and shear stresses from frictional and collisional components in the total stress. At low strain rates, frictional stress predominates while collisional stress remains minimal. As strain rates increase, collisional stress becomes the primary component, reflecting the transition from a solid-like to a fluid-like state in the granular material. The proposed phase transition model accurately captures these stress variations, effectively distinguishing solid-like and fluid-like behaviors.

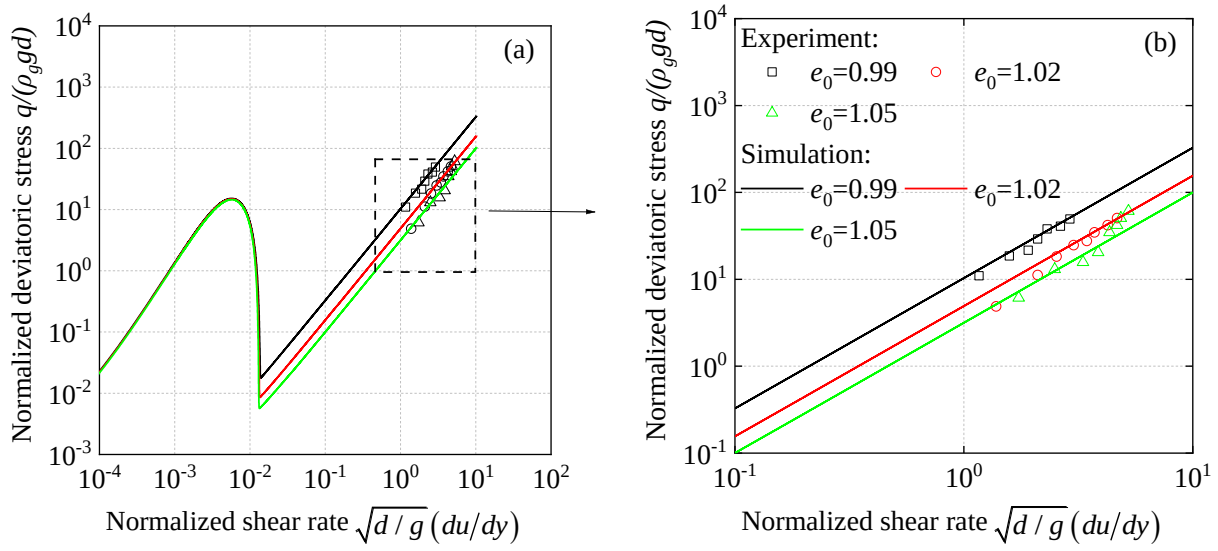

Fig 6. Comparison between numerical and experimental results for polystyrene beads: (a) A wide range of shear rate from 10^{-4} to 10^{2}; (b) A small range of shear rate from 0.1 to 10.

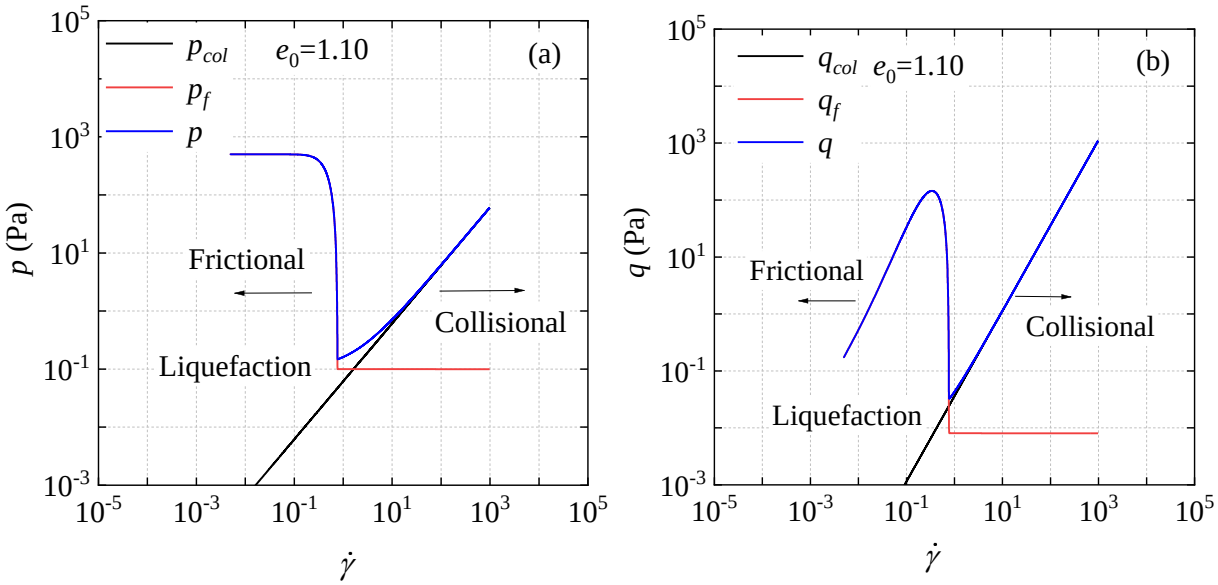

Fig 7. Comparison of different types of vertical and shear stresses in the undrained simple shear test for the specimen with e0=1.10: (a) Relation between the vertical stress and strain rate; (b) Relation between the shear stress and strain rate.

4 Numerical modeling of granular flow

In this section, we demonstrate the capability of the proposed phase transition model in modeling granular flows through two gravity-driven scenarios: the collapse of a sand column on a horizontal plane and a flume test. We particularly highlight and discuss the distinctions between the phase transition model and the conventional frictional stress model. All simulations were conducted on a PC equipped with an Intel® Core™ i9-13900K CPU @ 3.00 GHz and an NVIDIA® GeForce RTX™ 4080 with 16 GB RAM.

4.1 Column collapse on horizontal surface

4.1.1 Model definition and validation

To validate the proposed phase transition model and overall numerical scheme, we first examine a classical granular flow slumping on a flat surface, using the setup delineated by Bui et al. (2008). In this test, the granular material is initially packed into a column, resting at a solid-like state. When the gate is suddenly released, the collisional stress of the sand gradually increases, the material transitions to a fluid-like state. Fig. 8 (a) shows the initial profile of the granular column, with a height h_0 and basal distance d_0 (i.e., the aspect ratio is $a=h_0/d_0$). After the collapse, the sand forms a deposit with a profile characterized by the run-out distance d_∞ and deposit height h_∞ (see Fig. 8(b)).

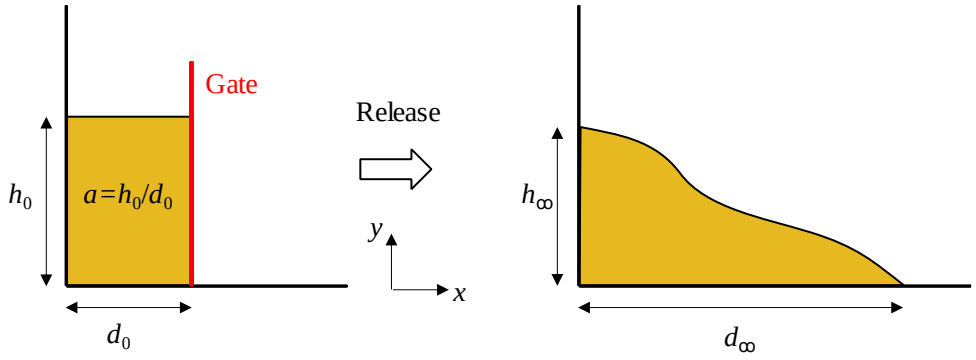

Fig 8. Illustration of the granular column before and after the collapse

Fig. 9 (a) illustrates the mesh and boundary conditions used in the MPM model for simulating granular column collapse under plane strain conditions. The soil sample is set to 20 cm in length and 10 cm in width, consistent with the experimental setup. Since the friction of the base layer

plays a marginal role in the column collapse (Fern and Soga, 2016), a no-slip boundary condition is adopted for the basal for simplicity. During simulations, constraints are applied to the degrees of freedom normal to the bottom and left sides of the domain. The domain is discretized using rectangular elements. A mesh sensitivity analysis is also performed to select an appropriate mesh resolution on collapse behavior, which is provided in Appendix C. As per the findings from the sensitivity analysis, a background grid size of 0.001 m is selected and each grid housing 4 material points. This setup results in a total of 80,000 material points. The time step is set as 1.0×10^{-5} s to guarantee the convergence. The total duration for the collapse process is 1 s. This simulation involves two steps. First, the lateral velocity on both sides of the column is constrained, allowing the sample to consolidate under gravity. Subsequently, the collapse is triggered by removing the horizontal constraint on the right side of the column. Fig. 9(b) presents the initial stress distribution for the sand column collapse, showing that the MPM model aligns closely with the initial geostress field, ranging from 0 to γgh along the depth. This consistency highlights the effectiveness of the MPM model.

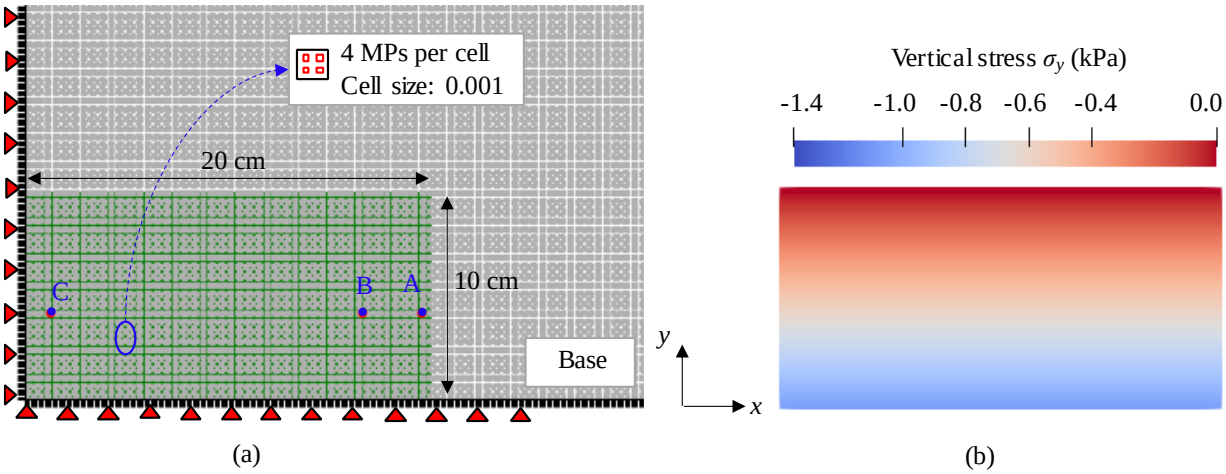

Fig 9. MPM setup condition and initial stress condition in modeling of granular column collapse: (a) Mesh and boundary conditions; (b) the initial stress distribution.

Table. 3 provides the basic parameters used for modeling the granular material. Parameters for the collisional stress part are based on the sand properties reported by Redaelli et al. (2017). An initial granular temperature of T_0=1.0·10^{-15} (Unit: 10^3 m^2/s^2) is selected to ensure that collisional stress remains negligible in the solid-like state before granular flow begins. Parameters for the frictional stress component are derived from the shear box tests reported by Bui et al. (2008) and

numerical analyses by Yin et al. (2018) and Zhu et al. (2024). The initial void ratio is set at 0.95, based on parameter analysis by Yin et al. (2018).

Fig. 10 (b) displays the free surface profile obtained from the simulation, wherein the run-out distance d_∞ is approximately 42 cm, and the deposit height h_∞ is around 10 cm, showing a good agreement with experimental results shown in Fig. 10 (a). The excellent agreement also underscores the joint effectiveness of MPM numerical modeling and the proposed phase transition model.

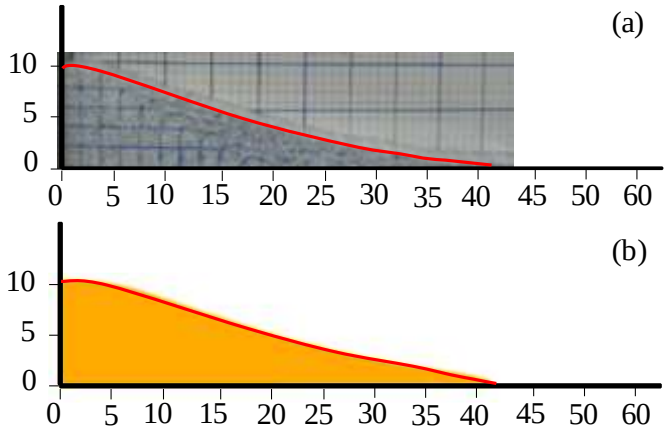

Fig 10. Comparison of the final free surface between experiment and MPM results: (a) experimental result by Bui et al. (2008); (b) MPM solution with the proposed phase transition model (Unit: cm)

4.1.2 Simulation results

Figs. 11 and 12 present the MPM results of the granular system collapse through four snapshots. The first snapshot at t=0.05 s shows the initial failure surface at the onset of the collapse. Subsequent snapshots at t=0.25 s and 0.5 s display the propagation of granular flow over time. And the last snapshot at t=1 s reveals the final deposition.

Fig. 11 depicts the evolution of the equivalent plastic strain and equivalent shear viscosity during the collapsing process. The equivalent plastic strain effectively delineates the boundary between quasi-static particles exhibiting minimal strain and mobilized particles experiencing significant strain. Notably, collisional stress is generated exclusively in mobilized areas characterized by large strain. The equivalent shear viscosity serves as an indicator of the evolving collisional stress and viscous properties of the granular flow.

Throughout the collapse, the granular material undergoes three distinct phases: initiation, propagation, and sedimentation. As this process unfolds, the frictional stress asymptotically approaches a limit value. Concurrently, the collisional stress demonstrates a non-monotonic trend, initially increasing from zero to a peak value before gradually diminishing to zero, as observed from Fig. 11 (b1) to Fig. 11 (b4). Fig. 11 (a1) demonstrates the rapid initiation of granular flow due to frictional failure near the column base. Particles in this region undergo significant deformation, as evidenced by equivalent shear plastic strain values approaching 1.0. Simultaneously, collisional stress gradually generates, represented by equivalent shear viscosity (Fig. 11 (b1)), albeit at relatively low magnitudes compared to later stages. As observed in Figs. 11 (a2) and (a3), illustrate the distinction between the mobilized zone, where material points reach a critical state and behave fluid-like, and the quasi-static zone, where material points remain solid-like. The interface between these zones delineates the transition from solid-like to fluid-like behavior. The solid-like state is predominantly governed by frictional stress, as evidenced by the absence of equivalent shear viscosity in the quasi-static area. In contrast, the fluid-like zone is influenced by both quasi-static and collisional stresses (see Fig. 11 (b2) and (b3). It can be seen that the rapid granular flow is associated with the increasing equivalent shear viscosity. Finally, the flow eventually ceases due to basal friction (see Fig. 11 (a4) and (b4)), with the equivalent shear viscosity η decreasing to zero, indicating a return to frictional stress dominance.

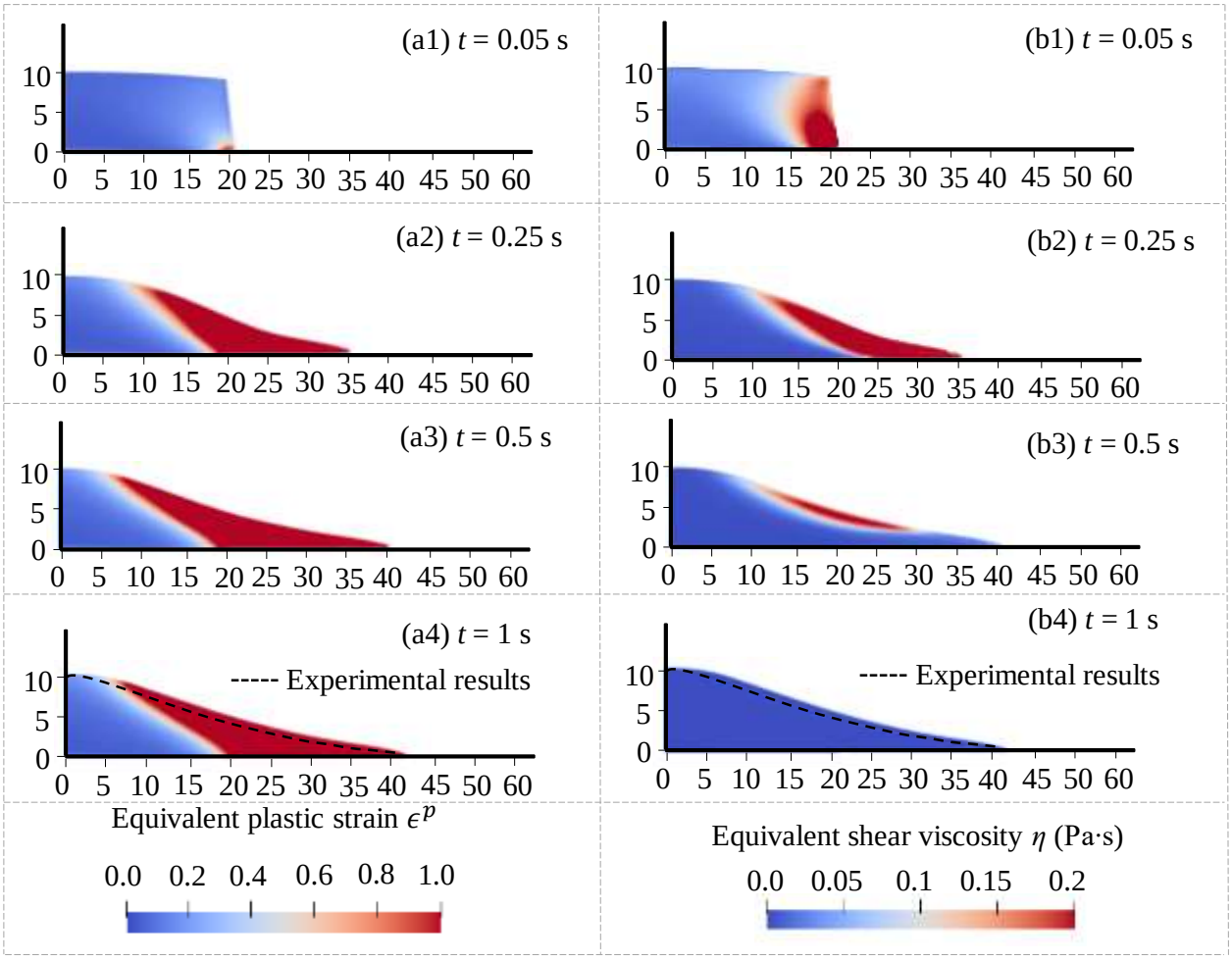

Fig 11. The equivalent plastic strain and bulk viscosity in the column collapse problem: (a) the evolution of the equivalent plastic strain; (b) the evolution of the equivalent shear viscosity.

Fig.12 illustrates the evolution of the state variable granular temperature T during the collapse. As observed, granular temperature T initially increases and then decreases, aligning with the evolution of the equivalent shear viscosity. When the granular temperature is near zero, granular material is in solid-like state. While the granular temperature increases, the material evolves into the fluid-like state. Although the granular temperature in the front of the flow is zero, that of the middle upper part is still high, indicating that the middle upper part is still fluid-like behavior. These findings indicate that the state variable granular temperature can effectively depict the evolution of collisional stress in granular flow.

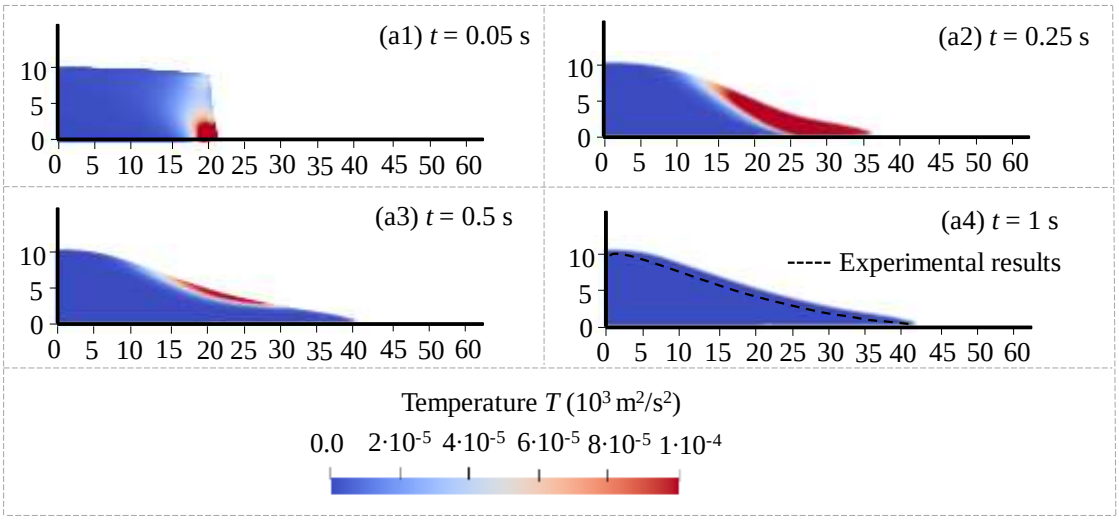

Fig 12. Evolution of the granular temperature *T* in the system.

To further elucidate the evolution of collisional stress during the collapse, three material points were tracked throughout the simulation. The initial positions of these points are illustrated in Fig. 9. Particle C is situated deepest within the sand column, Particle A is located near the free surface and is subject to larger deformation, while particle B occupies an intermediate position between A and C.

Fig.13 depicts the evolution of two critical parameters for the three tracked particles: the collisional stress percentage K_{col} in the total deviatoric stress and the deviatoric strain rate increment. K_{col} is defined as $K_{col} = q_{col} \big/ \left(q_{col} + q_f \right)$, where q_{col} and q_f are the deviatoric collisional and frictional stress, respectively. The K_{col} ranges from 0 to 1, indicating purely solid-like (frictional stress-dominated) to purely fluid-like (collisional stress-dominated) behavior, respectively.

During the granular flow, the percentage of collisional stress K_{col} of particle A is larger than particle B, with that of particle C being the smallest, indicating that particles near the free surface are easier to form fluid-like behavior. The percentage of collisional stress K_{col} of particle C is near zero, its corresponding stain rate is also near zero. The large K_{col} of particles A and B appear at the large stain rate zone. It indicates that the fluid-like behavior appears at the large stain rate zone and the solid-like behavior appears at the small stain rate zone, which exactly reflects the effectiveness of the proposed model.

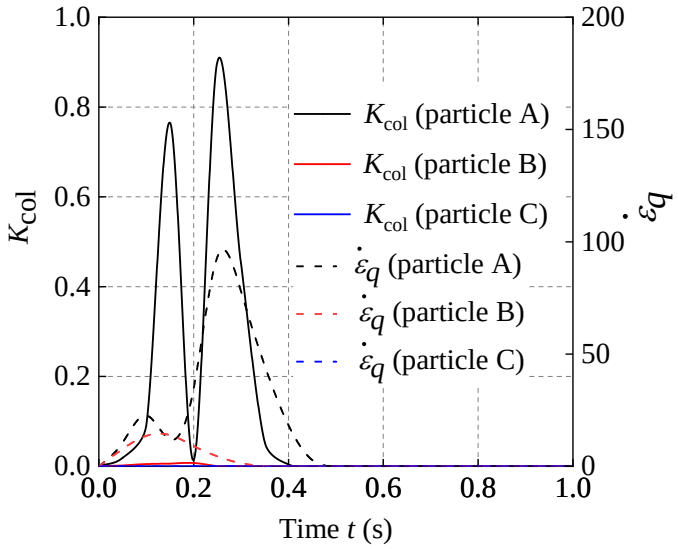

Fig 13. Change in percentage of collisional stress part in the total stress at three particles in the column collapse

To further elucidate the collisional stress of the individual particle, we also analyze the evolution of the deviatoric collisional stress and its corresponding temperature of particles A and B (see Figs. 14). Three distinct stages in the collapse process are identified: initiation, propagation, and sedimentation. Stage I is characterized by the absence of collisional stress, indicating solid-like behavior. As the granular material reaches a critical state, it transitions into Stage II, marked by the emergence of collisional stress. During this stage, both collisional and frictional stresses coexist, resulting in fluid-like behavior. Stage III sees the dissipation of collisional stress, with only frictional stress remaining, signifying a return to solid-like behavior. Compared between Fig. 14 (a) and Fig. 14 (b), the duration for Stage I is very short, indicating the initiation of granular flow is rapid. In addition, it is observed particles closer to the surface maintain fluid-like behavior for longer periods. The evolution of granular temperature closely mirrors that of collisional stress for both particles, and also suggests the fundamental role of granular temperature T in governing material phase transitions.

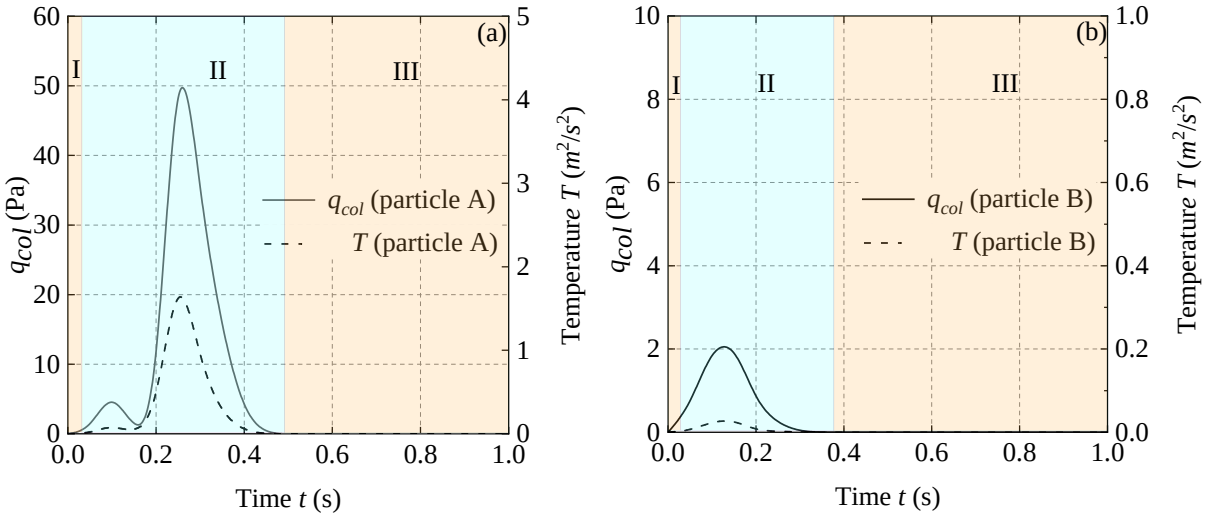

Fig 14. The evolution of the collisional stress and temperature for particles A and B in the column collapse: (a) Evolution of particle A; (c) Evolution of particle B.

4.1.3 Comparison against purely frictional solid-like model

To highlight the necessity of consideration of phase transition, we conducted a comparative analysis with a frictional solid-like model, which employs only frictional stress based on the critical-state elastoplasticity framework to compute the governing stress during MPM simulations. It is important to note that the individual collisional stress model cannot be employed to simulate the entire flow process, as the temperature-controlled collisional stress is too minimal during initiation to sustain the material volume.

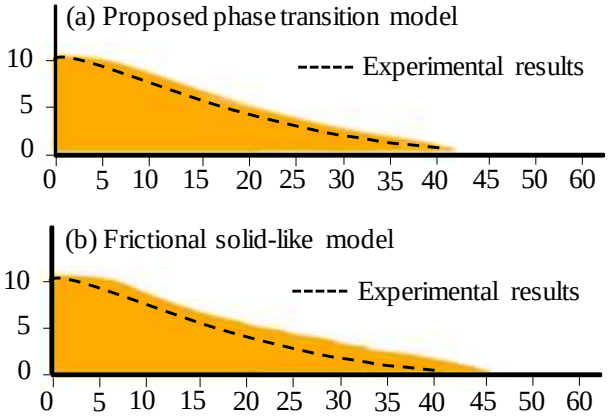

Fig 15. Comparison of the final free surface between the proposed phase transition model and frictional solid-like model: (a) result by proposed phase transition model; (b) result by the frictional solid-like model (Unit: cm)

Fig. 15 compares the final free surface obtained from the phase transition model with that from the frictional solid-like model. The findings indicate that the phase transition model yields a

smaller run-out distance and the purely frictional stress model overestimates the final depositional morphology from experimental results, attributed to the fact that resistance against the forward mobilization in the phase transition model is higher than the frictional solid-like model. Fig.16 compares the velocity contours of the two models. At 0.5 seconds, the phase transition model exhibits nearly zero velocity, while the frictional solid-like model maintains a velocity close to 0.2 m/s. This is because the phase transition model considers the additional viscosity in fluid-like collisional stress, resulting in lower forward velocity, supporting the observations in Fig.15. Fig.17 contrasts the equivalent plastic strain. The similarity in strain contours indicates that frictional interactions predominantly govern particle behavior.

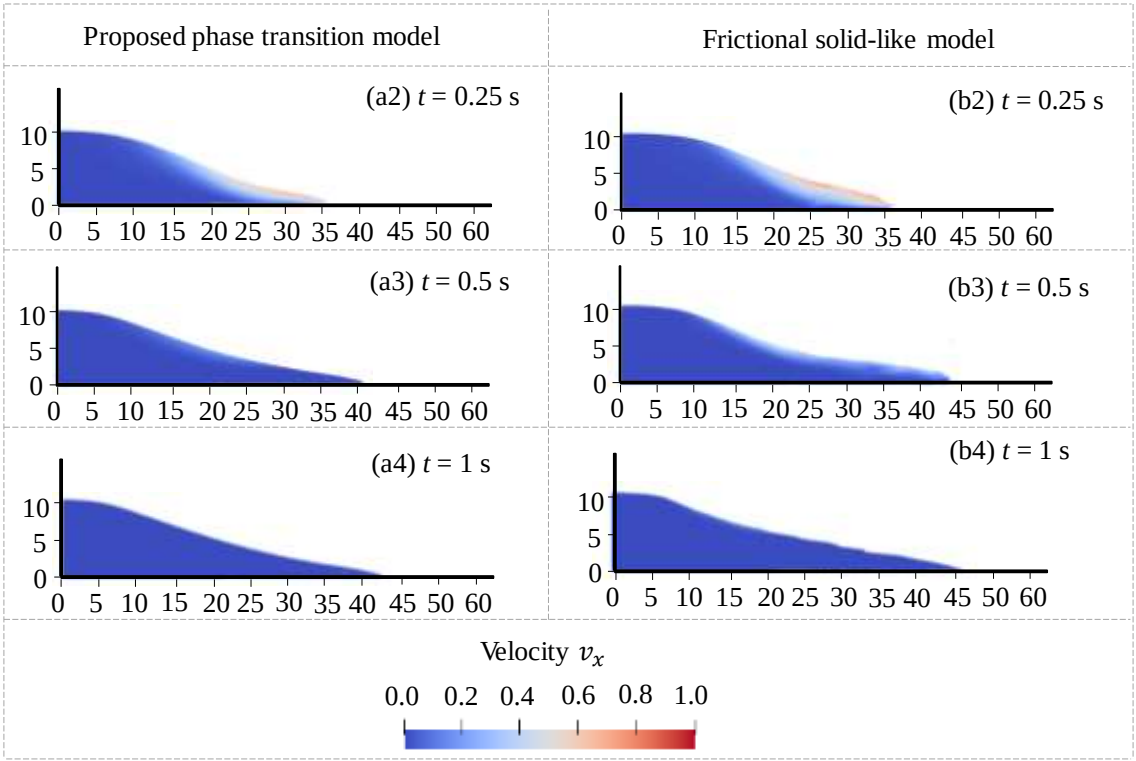

Fig 16. Comparison of the velocity v_x between different models: (a) Result by proposed phase transition model; (b) Result by the frictional solid-like model (Unit: m/s).

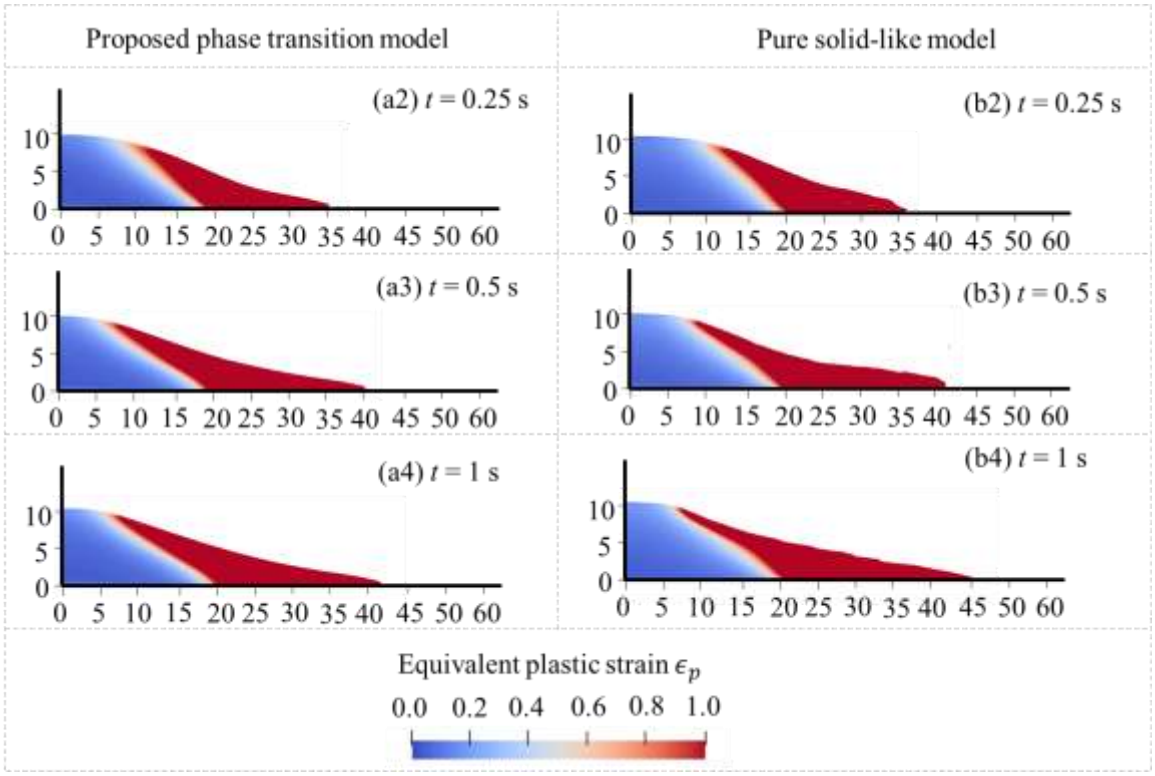

Fig 17. Comparison of equivalent plastic strain between different models: (a) result by proposed phase transition model; (b) result by the frictional solid-like model

4.2 Flume test on inclined surface

4.2.1 Model setup

In this section, the flume test is employed to investigate the behavior of the granular material transition from a solid-like to fluid-like state. The flume test can generate the granular flow with a faster velocity and longer duration, where the collisional stress plays a significant role. We refer to the experimental investigation of granular flows on an inclined surface reported by Moriguchi et al. (2009) for the current study. In the prototype experiment, a total mass of 50.0 kg of dry sand is initially confined in a box at the top of the flume with an inclination of 45°. The box gate is suddenly opened to release the sand. The length and width of the box are set as 50 cm and 30 cm, respectively. The length of the slope is reported as 230 cm.

Fig.18 (a) shows the mesh and boundary conditions of the flume test, which has the same setup as the experiment. This study employs a no-slip boundary condition for the rough base layer, as recommended by Moriguchi et al. (2009). Specifically, both vertical and horizontal velocities

are constrained at the inclined boundaries during simulation. As illustrated in Fig.18(a), nodes (e.g., Nodes *i*, *j*, *k*) beneath the inclined boundary in the structured grid are identified based on the inclination angle, with their vertical and horizontal velocities set to zero. Note that this study focuses on developing a novel constitutive model that considers phase transition. Recognizing the importance of accurately addressing complex boundary conditions, future work will extend the current model to incorporate these complexities within the MPM framework via an effective algorithm (e.g., Liang et al., 2024). It is crucial to emphasize that the primary aim of this study is to analyze granular flow dynamics, rather than simulating the impact process on the load cell at the terminus of the inclined surface as observed in the prototype experiment. Instead, the simulation is extended to include flow on a flat surface beyond the inclined plane, enabling a comprehensive analysis of the entire flow evolution. Fig. 5(b) displays the initial stress distribution for the slump test, where vertical stress exhibits a nearly linear increase with depth. At the deepest point, the vertical stress approaches -5 kPa, aligning well with γgh and further confirming the model's accuracy.

A mesh sensitivity analysis is carried out to choose a rational mesh approach (see Appendix. C). Based on the results, a rectangular element with 4 material points and a background grid size of 0.005 m are adopted to discretize the material domain. The total number of the particles is 12,800. To guarantee calculation convergence, the time step is set as 1.0×10^{-6} s. The total time of the granular flow is 3 s. The basic parameters employed in this simulation are shown in Table. 3.

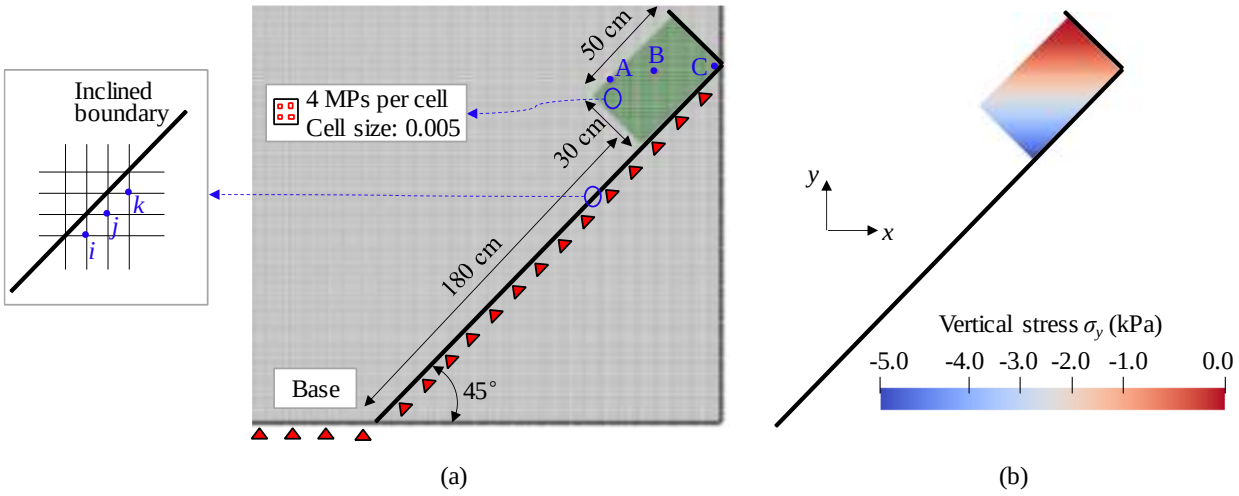

(a) (b)

Fig 18. MPM setup condition and initial stress condition in modeling of flume test: (a) Mesh and boundary conditions; (b) the initial stress distribution.

4.2.2 Simulation results

Fig. 19 shows the comparison of snapshots of granular materials on the steep slope between the experimental and numerical results. At t=0.4 s, the granular material exhibits a distinctive behavior characterized by rapid movement of the front portion while the rear segment remains within the initial confinement. A notable granular heap formation is observed. The MPM solution (see Fig. 19 (b1)) has a run-out distance (d_∞) of around 125 cm and a maximum deposit height (h_∞) of approximately 10 cm. At t=0.8 s, the granular material quickly moves forward in a fluid-like state. The MPM solution (see Fig. 19 (b2)) has a run-out distance (d_∞) of around 215 cm. The deposit heap gradually flattens. The free surfaces from MPM match the experimental results by Moriguchi et al. (2009) well, which indicates the effectiveness of the proposed MPM modeling scheme with the proposed phase transition model.

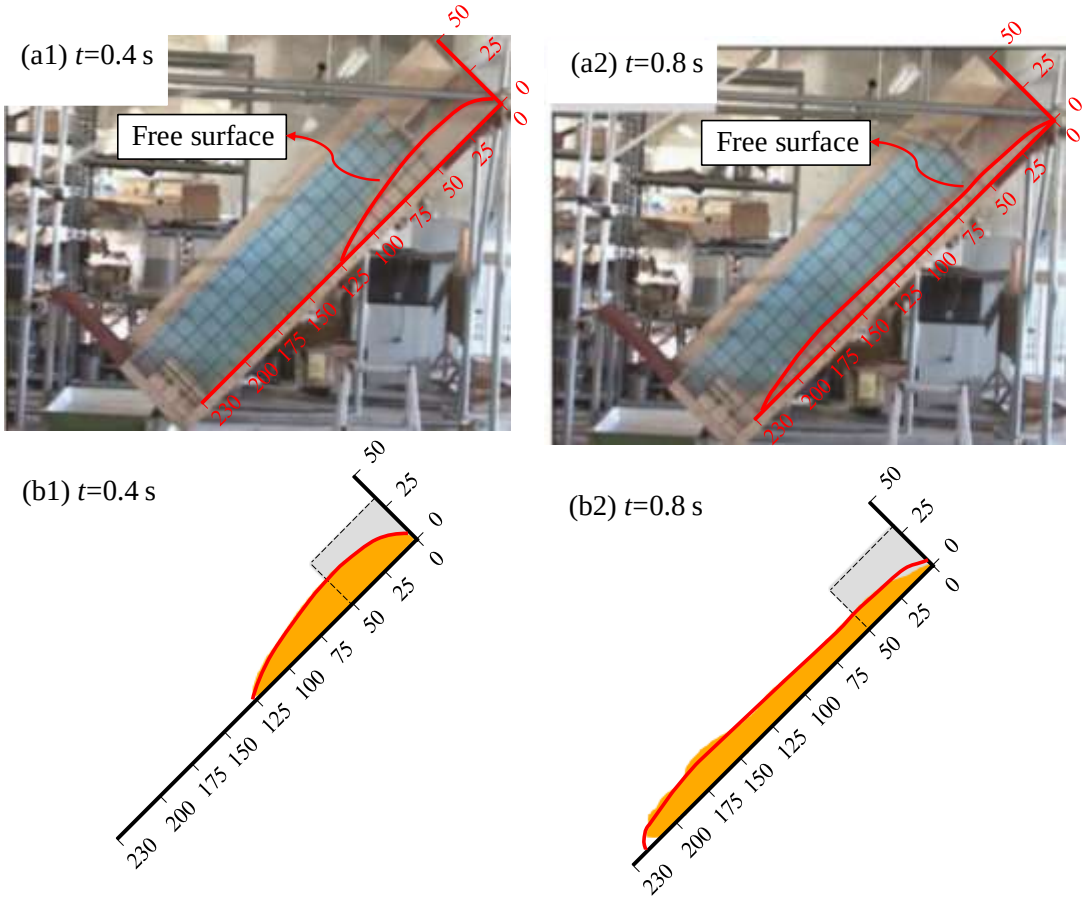

Fig 19. Comparison of the final free surface between experiment results and MPM simulation: (a) experimental result; (b) MPM solution with the proposed phase transition model (Unit: cm)

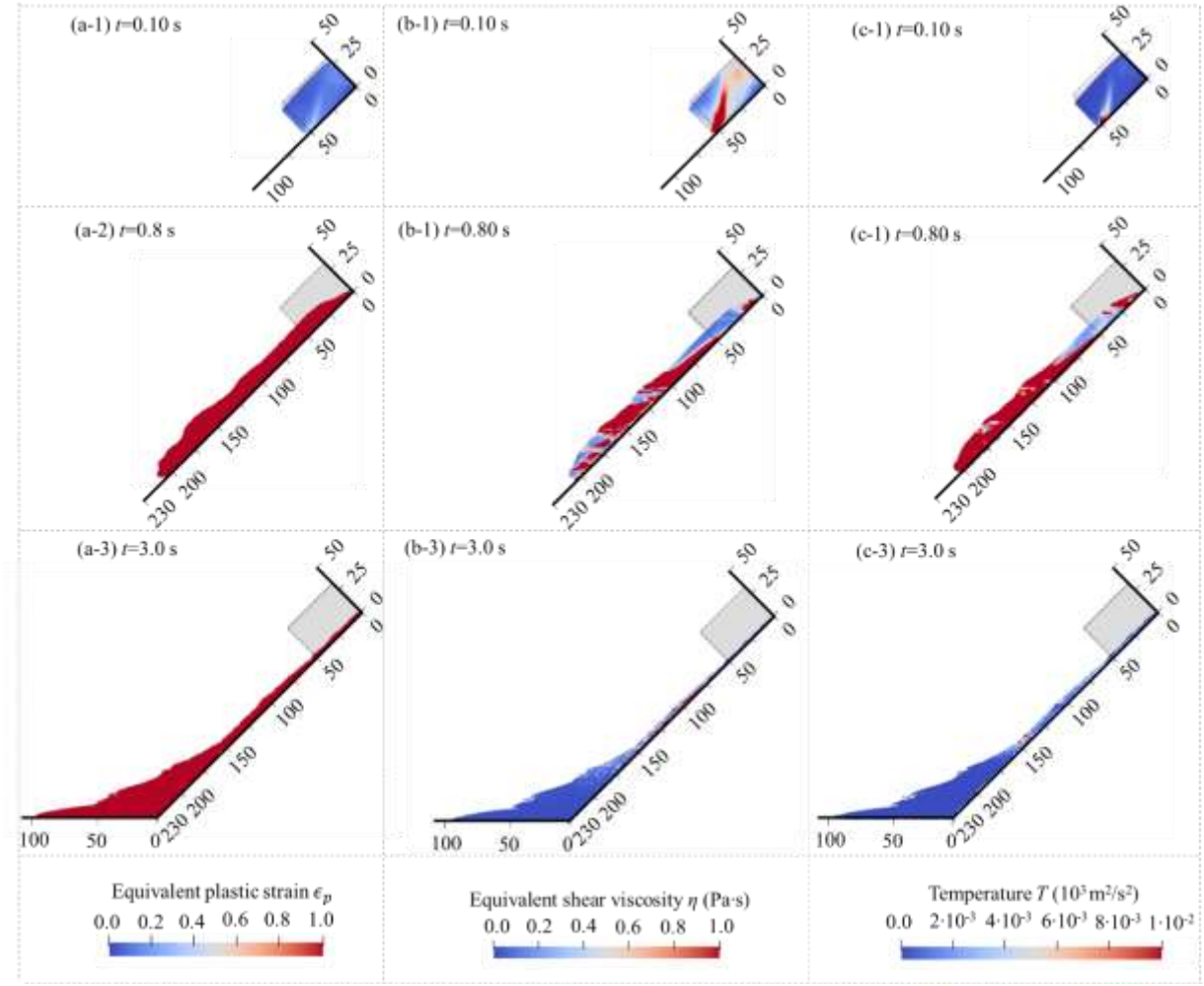

Fig 20. The equivalent plastic strain, shear viscosity, and granular temperature in the slump test problem: (a) the evolution of the equivalent plastic strain; (b) the evolution of the equivalent shear viscosity; (c) the evolution of the granular temperature *T*.

Fig. 20 presents the evolution of the equivalent plastic strain, shear viscosity, and granular temperature in the slump test at t = 0.1 s, 0.8 s, and 3 s, clearly demonstrating the model's ability to depict collisional stress evolution through the granular temperature state variable and the phase transition process. However, the evolution patterns of equivalent shear viscosity and granular temperature differ from those observed in the sand column collapse on a horizontal surface (see Figs. 11 and 20). In the fluid-like stage of the flume test, the model exhibits higher equivalent shear viscosity, generated by collisional stress, to resist the faster velocity, indicating that swifter granular flow engenders higher collisional stress. Figs.20 (b-1) and (c-1) show unsteady equivalent shear viscosity and granular temperature, suggesting that faster granular flow produces a more unstable fluid-like state. Notably, there are discontinuities in equivalent shear viscosity and granular temperature. These could be attributed to two factors: (i) cell-crossing errors occurring as material

points traverse cell boundaries, potentially contributing to numerical errors in modeling fast granular flow, and (ii) the kinetic theory treating sand particles as rigid bodies in the fluid-like state, further contributing to the discontinuity. Despite these discontinuities, the phase transition model effectively captures the granular flow behavior from solid- to fluid-like state.

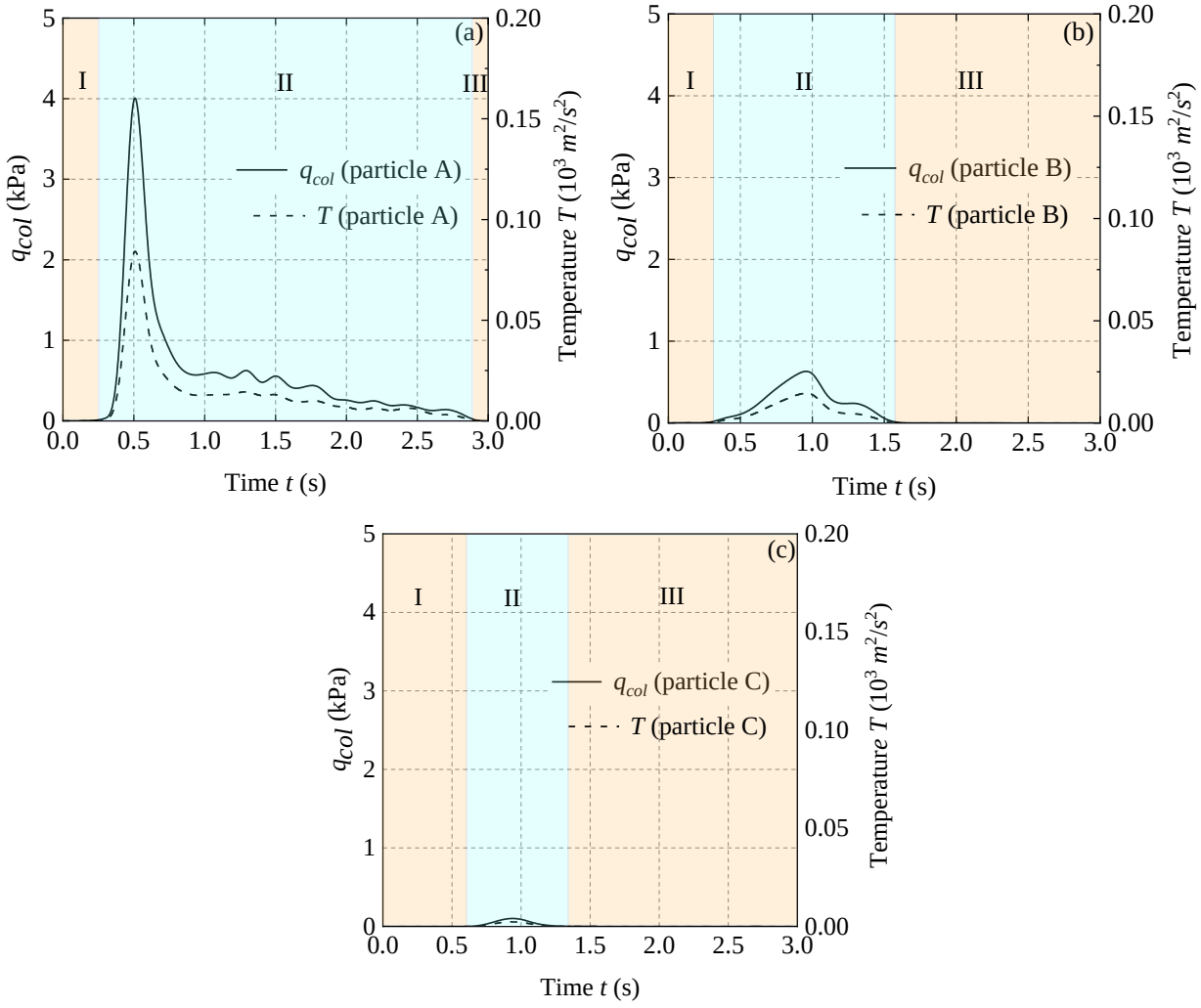

Fig 21. The evolution of the collisional stress and temperature for particle A, B, and C in the slump test

Three material points are tracked during the MPM simulation of the flume test. The initial position of the three points is shown in Fig. 18(a). Particle C is located near the inside corner of the box. Particle A is close to the top surface. Particle B is between A and C. The time increment for each marker is 0.1 s. The analysis of these three points illustrates the behavior of the granular particles in the granular flow. Fig. 21 further shows the evolution of the deviatoric part of the collisional stress and its corresponding temperature of the three particles. The evolution of the collisional stresses of both three particles matches well with the granular temperature, which once

again indicates that the state variable temperature fundamentally governs the evolution of collisional stresses, further controlling the material phase transition. All three particles have three stages. As mentioned before, stages I and III describe the solid-like state of the granular material. The time distinguishing stage I and II is the initiation of the granular flow. Stage II depicts the fluid-like state. It is evident that particle A has the longest fluid-like state and smallest initiation time, and particle C has the shortest fluid-like state and largest initiation time, which demonstrates that the particle near the surface has a longer time in a fluid-like state.

4.2.3 Comparison against purely frictional solid-like model

We further compare the results of the phase transition model and the frictional solid-like model (see Figs. 22 and 23). Fig. 22 shows the equivalent plastic strain contours, indicating that nearly all particles undergo plastic deformation under faster swifter granular flow. Fig. 23 presents the velocity contours of the two models. At 0.8 s, the phase transition model exhibits a higher but narrower deposition front compared to the frictional solid-like model due to the viscosity in the phase transition model, which resists shape changes and relative movement between particles. At 3 s, the frictional solid-like model demonstrates a longer run-out distance than the phase transition model, further emphasizing the importance of considering phase transitions.

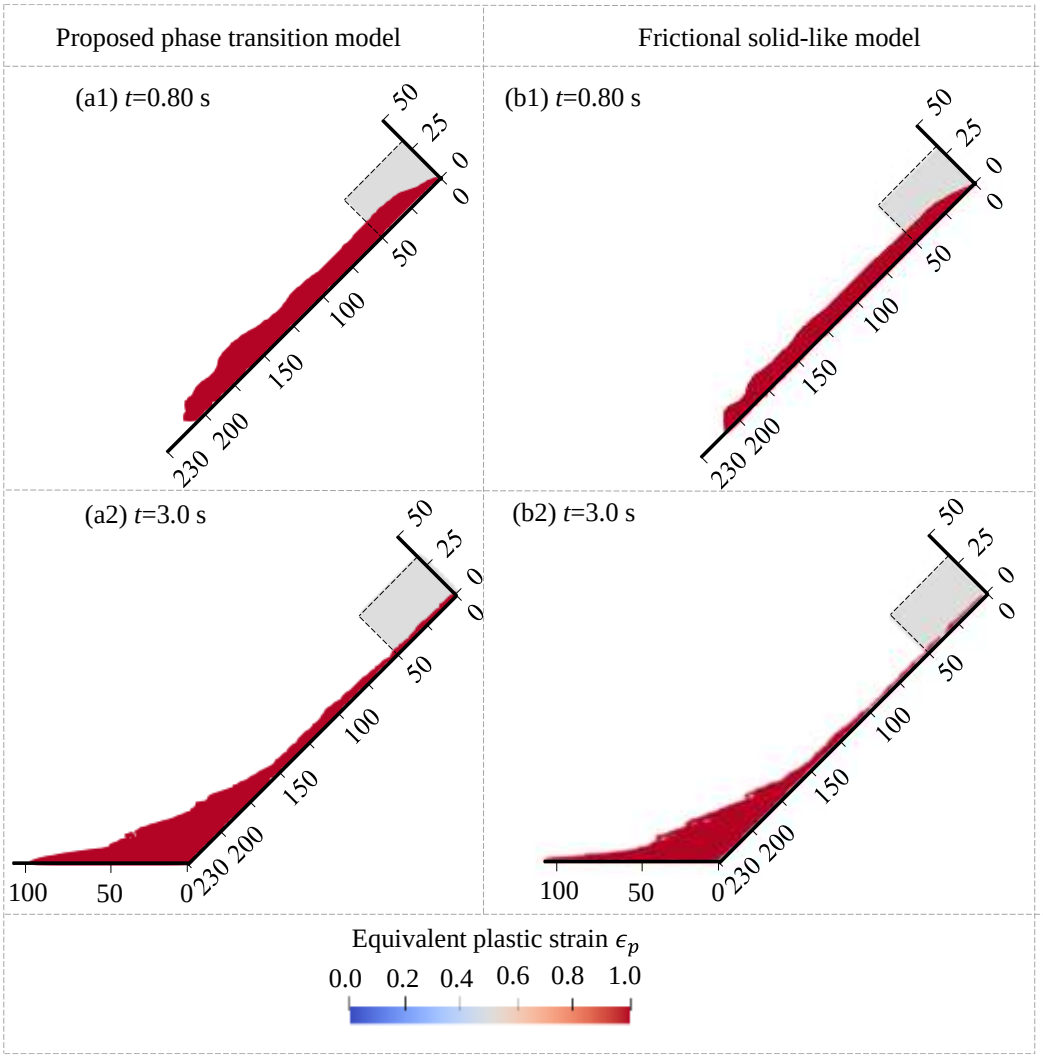

Fig 22. Comparison of equivalent plastic strain between different models: (a) result by proposed phase transition model; (b) result by the frictional solid-like model

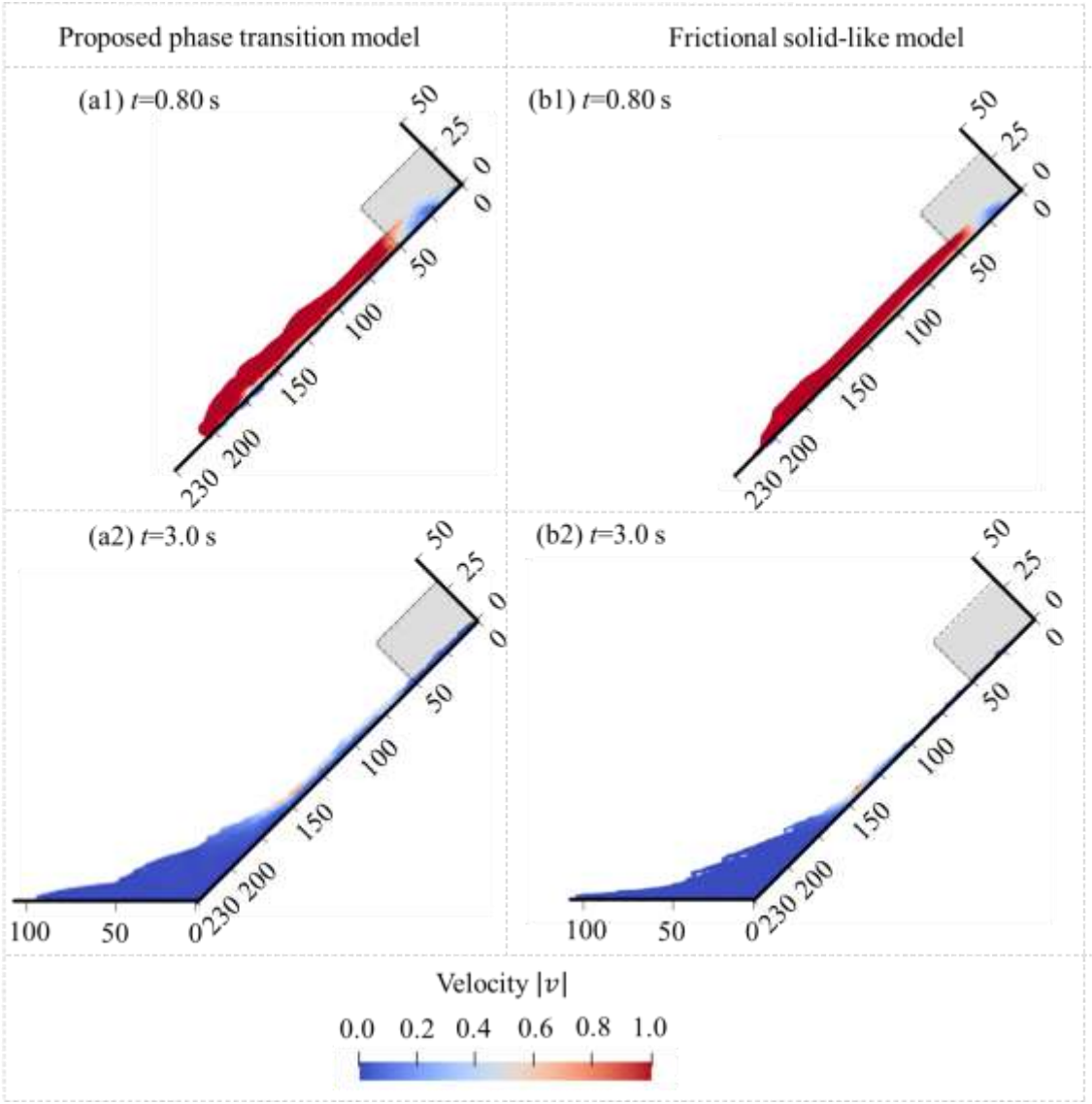

Fig 23. Comparison of the total velocity $|v|$ between different models: (a) Result by proposed phase transition model; (b) Result by the frictional solid-like model (Unit: m/s)

5 Conclusions

This study introduces a novel phase transition model within the MPM framework to simulate granular flow, effectively capturing the transition of granular material from a solid-like to a fluid-like state. The proposed elastoplasticity-based phase transition model is established by combining the frictional and collisional stress to consider both the friction and collision mechanisms in granular flow, respectively. The frictional stress is expressed using a critical-state-based elasto-plastic model characterized by nonlinear elasticity, nonlinear plastic hardening, and stress dilatancy. The collisional stress is described via a well-established kinetic theory, whose state variable

granular temperature fundamentally governs the material phase transition. The proposed phase transition model is further incorporated into the GPU-based MPM for modeling with the novel phase transition model is applied to the granular column collapses on a horizontal surface and slump test on an inclined plane. The following observations have been made:

(1). The numerical results on the granular flows agree well with the available experimental data, indicating the effectiveness of the proposed phase transition model.

(2) When the granular material is in a solid-like state, the frictional stress is predominant, while the collisional stress plays a significant role for granular materials in a fluid-like state. The proposed phase transition model can predict these features nicely.

(3) From initiation, propagation, and sedimentation, the collisional stress experiences a rapid increase followed by a gradual decrease. The state variable granular temperature fundamentally governs the phase transition.

(4) Both numerical results of the granular column collapse and slump test show the particles close to the surface stay in a fluid-like state for a longer duration and transition faster. A comparison reveals that a swifter granular flow engenders a higher collisional stress and a more unstable fluid-like state.

Acknowledgments

This research is financially supported by Open Research Fund Program of State key Laboratory of Hydroscience and Engineering (Grant No.: sklhse-2023-D-05), Open Research Fund Program of Key Laboratory of the Hydrosphere of the Ministry of Water Resources (Grant No.: mklhs-2023-05) and the Research Grants Council (RGC) of Hong Kong Special Administrative Region Government (HKSARG) of China (Grant No.: 15226322, 15229223, 15232224).

Data availability statements

The datasets generated during and/or analyzed during the current study are available from the corresponding author on reasonable request.

References

Ancey, C. (2007). Plasticity and geophysical flows: A review. Journal of Non-Newtonian Fluid Mechanics, 142(1-3), 4-35. https://doi.org/10.1016/j.jnnfm.2006.05.005

Augarde, C. E., Lee, S. J., & Loukidis, D. (2021). Numerical modelling of large deformation problems in geotechnical engineering: A state-of-the-art review. Soils and Foundations, 61(6), 1718-1735. https://doi.org/10.1016/j.sandf.2021.08.007

Bai, L., Zheng, Q. J., & Yu, A. B. (2017). FEM simulation of particle flow and convective mixing in a cylindrical bladed mixer. Powder Technology, 313, 175-183.

Berzi, D., di Prisco, C., & Vescovi, D. (2011). Constitutive relations for steady, dense granular flows. Physical Review E, 84, 031301.

Bocquet, L., Errami, J., & Lubensky, T. C. (2002). Hydrodynamic model for a dynamical jammed-to-flowing transition in gravity driven granular media. Physical Review Letters, 89(18). https://doi.org/10.1103/PhysRevLett.89.184301

Bui, H. H., Fukagawa, R., Sako, K., & Ohno, S. (2008). Lagrangian meshfree particles method (SPH) for large deformation and failure flows of geomaterial using elastic–plastic soil constitutive model. International Journal for Numerical and Analytical Methods in Geomechanics, 32(12), 1537-1570. https://doi.org/10.1002/nag.688

Cante, J., Davalos, C., Hernandez, J. A., Oliver, J., Jonsén, P., Gustafsson, G., & Häggblad, H. Å. (2014). PFEM-based modeling of industrial granular flows. Computational Particle Mechanics, 1, 47-70.

Cascini, L., Cuomo, S., Pastor, M., & Rendina, I. (2016). SPH-FDM propagation and pore water pressure modelling for debris flows in flume tests. Engineering Geology, 213, 74-83. https://doi.org/10.1016/j.enggeo.2016.08.007

Ceccato, F., & Simonini, P. (2016). Granular flow impact forces on protection structures: MPM numerical simulations with different constitutive models. Procedia Engineering, 158, 164-169.

Chang, C. S., & Yin, Z. Y. (2010). Modeling stress-dilatancy for sand under compression and extension loading conditions. Journal of Engineering Mechanics-ASCE, 136(6), 777-786. https://doi.org/10.1061/(ASCE)EM.1943-7889.0000116

Chen, F. Z., & Yan, H. (2021). Constitutive model for solid-like, liquid-like, and gas-like phases of granular media and their numerical implementation. Powder Technology, 390, 369-386. https://doi.org/10.1016/j.powtec.2021.05.023

Chialvo, S., & Sundaresan, S. (2013). A modified kinetic theory for frictional granular flows in dense and dilute regimes. Physics of Fluids, 25(7), 070303. https://doi.org/10.1063/1.4812804

Cremonesi, M., Franci, A., Idelsohn, S., & Oñate, E. (2020). A state of the art review of the particle finite element method (PFEM). Archives of Computational Methods in Engineering, 27(5), 1709-1735.

Cuomo, S., Ghasemi, P., Martinelli, M., & Calvello, M. (2019). Simulation of liquefaction and retrogressive slope failure in loose coarse-grained material. International Journal of Geomechanics, 19(10). https://doi.org/10.1061/(ASCE)GM.1943-5622.0001500

Dai, Z. L., Huang, Y., Cheng, H. L., & Xu, Q. (2014). 3D numerical modeling using smoothed particle hydrodynamics of flow-like landslide propagation triggered by the 2008 Wenchuan earthquake. Engineering Geology, 180, 21-33. https://doi.org/10.1016/j.enggeo.2014.03.018

Di Carluccio, G., Pinyol, N. M., Alonso, E. E., & Hürlimann, M. (2024). Liquefaction-induced

818 flow-like landslides: The case of Valarties (Spain). Géotechnique, 74(4), 307-324.
819 https://doi.org/10.1680/jgeot.21.00112
820 Dong, Y. K., & Grabe, J. (2018). Large scale parallelisation of the material point method with
821 multiple GPUs. Computers and Geotechnics, 101, 149-158.
822 https://doi.org/10.1016/j.compgeo.2018.04.001
823 Dong, Y. K., Wang, D., & Randolph, M. F. (2015). A GPU parallel computing strategy for the
824 material point method. Computers and Geotechnics, 66, 31-38.
825 https://doi.org/10.1016/j.compgeo.2015.01.009
826 Dunatunga, S., & Kamrin, K. (2015). Continuum modelling and simulation of granular flows
827 through their many phases. Journal of Fluid Mechanics, 779, 483-513.
828 https://doi.org/10.1017/jfm.2015.383
829 Faroux, D., Washino, K., Tsuji, T., & Tanaka, T. (2022). A FVM implementation and validation of
830 non-local modeling for single-and two-phase granular flows. Computational Particle
831 Mechanics, 1-15.
832 Feng, H., Huang, M. S., Shi, Z. H., Shen, K. M., & Wang, B. (2024). Macro-element modeling of
833 suction caisson subjected to vertical tensile loading via up-scaling soil stress-strain relations.
834 Ocean Engineering, 304. https://doi.org/10.1016/j.oceaneng.2024.117850
835 Fern, E. J., & Soga, K. (2016). The role of constitutive models in MPM simulations of granular
836 column collapses. Acta Geotechnica, 11(3), 659-678. https://doi.org/10.1007/s11440-016-
837 0436-x
838 Franci, A., & Cremonesi, M. (2019). 3D regularized μ(I)-rheology for granular flows simulation.
839 Journal of Computational Physics, 378, 257-277. https://doi.org/10.1016/j.jcp.2018.11.011
840 Garzó, V., & Dufty, J. W. (1999). Dense fluid transport for inelastic hard spheres. Physical Review
841 E, 59, 5895-5911.
842 Guo, X., Peng, C., Wu, W., & Wang, Y. (2016). A hypoplastic constitutive model for debris
843 materials. Acta Geotechnica, 11(6), 1217-1229. https://doi.org/10.1007/s11440-016-0494-
844 0.
845 Guo, X., Peng, C., Wu, W., & Wang, Y. (2020). Unified constitutive model for granular–fluid
846 mixture in quasi-static and dense flow regimes. Acta Geotechnica, 16(3), 775-787.
847 https://doi.org/10.1007/s11440-020-01044-1
848 Haeri, A., & Skonieczny, K. (2022). Three-dimensional granular flow continuum modeling via
849 material point method with hyperelastic nonlocal granular fluidity. Computer Methods in
850 Applied Mechanics and Engineering, 394, 114904.
851 Hayat, T., Momani, S., & Muhammad, K. (2021). FDM analysis for nonlinear mixed convective
852 nanofluid flow with entropy generation. International Communications in Heat and Mass
853 Transfer, 126, 105389.
854 He, K. Y., Jin, Y. F., Zhou, X. W., & Yin, Z. Y. (2024). A high-performance semi-implicit two-phase
855 two-layer MPM framework for modeling granular mass-water interaction problems.
856 Computer Methods in Applied Mechanics and Engineering, 427, 117064.
857 Hu, Y., Li, T. M., Anderson, L., Ragan-Kelley, J., & Durand, F. (2019). Taichi: A language for high-
858 performance computation on spatially sparse data structures. ACM Transactions on
859 Graphics (TOG), 38(6), 1-16.
860 Huang, Y., Zhang, W. J., Mao, W. W., & Jin, C. (2011). Flow analysis of liquefied soils based on
861 smoothed particle hydrodynamics. Natural Hazards, 59(3), 1547-1560.
862 https://doi.org/10.1007/s11069-011-9851-3
863 Hurley, R. C., & Andrade, J. E. (2017). Continuum modeling of rate-dependent granular flows in
864 SPH. Computational Particle Mechanics, 4(1), 119-130. https://doi.org/10.1007/s40571-

016-0132-5
Jaeger, H. M., Nagel, S. R., & Behringer, R. P. (1996). Granular solids, liquids, and gases. Reviews of Modern Physics, 68(4), 1259-1273. https://doi.org/10.1103/RevModPhys.68.1259
Jenkins, J. T., & Savage, S. B. (1983). A theory for the rapid flow of identical, smooth, nearly elastic, spherical particles. Journal of Fluid Mechanics, 130, 187-202.
Jenkins, J. T., & Zhang, C. (2002). Kinetic theory for identical frictional, nearly elastic spheres. Physics of Fluids, 14, 1228-1235.
Jenkins, J. T. (2006). Dense shearing flows of inelastic disks. Physics of Fluids, 18, 103307.
Jenkins, J. T. (2007). Dense shearing flows of inelastic spheres. Granular Matter, 10, 47-52.
Jin, Y. F., Wu, Z. X., Yin, Z. Y., & Shen, J. S. (2017). Estimation of critical state-related formula in advanced constitutive modeling of granular material. Acta Geotechnica, 12(6), 1329-1351. https://doi.org/10.1007/s11440-017-0586-5
Johnson, P. C., & Jackson, R. (1987). Frictional-collisional constitutive relations for granular materials, with application to plane shearing. Journal of Fluid Mechanics, 176, 67-93. https://doi.org/10.1017/S0022112087000570
Johnson, P. C., Nott, P., & Jackson, R. (1990). Frictional collisional equations of motion for particulate flows and their application to chutes. Journal of Fluid Mechanics, 210, 501-535. https://doi.org/10.1017/S0022112090001380
Kim, S., & Kamrin, K. (2023). A second-order non-local model for granular flows. Frontiers in Physics, 11, 1092233.
Lagrée, P. Y., Staron, L., & Popinet, S. (2011). The granular column collapse as a continuum: Validity of a two-dimensional Navier–Stokes model with a μ(I)-rheology. Journal of Fluid Mechanics, 686, 378-408. https://doi.org/10.1017/jfm.2011.335
Larsson, S., Rodríguez Prieto, J. M., Gustafsson, G., Häggblad, H. Å., & Jonsén, P. (2021). The particle finite element method for transient granular material flow: Modelling and validation. Computational Particle Mechanics, 8, 135-155.
Lee, C. H., & Huang, C. J. (2010). Model of sheared granular material and application to surface-driven granular flows under gravity. Physics of Fluids, 22(4).
Lei, X., Chen, X., Yang, Z., He, S., Zhu, L., & Liang, H. (2022). A simple and robust MPM framework for modelling granular flows over complex terrains. Computers and Geotechnics, 149, 104867.
Lin, C. C., & Yang, F. L. (2020). Continuum simulation for regularized non-local μ(I) model of dense granular flows. Journal of Computational Physics, 420, 109708.
Louge, M. Y. (2003). Model for dense granular flows down bumpy inclines. Physical Review E, 67, 061303.
Liang, W., & Zhao, J. (2019). Multiscale modeling of large deformation in geomechanics. International Journal for Numerical and Analytical Methods in Geomechanics, 43(5), 1080-1114.
Liang, W., He, K. Y., Jin, Y. F., & Yin, Z. Y. (2024). A gradient-smoothed material point method for reducing cell crossing noise in large deformation problems. Computers and Geotechnics, 169, 106169.
Liang, W., Zhao, J., Wu, H., & Soga, K. (2023). Multiscale, multiphysics modeling of saturated granular materials in large deformation. Computer Methods in Applied Mechanics and Engineering, 405, 115871.
Liang, W., Fang, H., Yin, Z. Y., & Zhao, J. (2024). A mortar segment-to-segment frictional contact approach in material point method. Computer Methods in Applied Mechanics and Engineering, 431, 117294.

Jop, P., Forterre, Y., Pouliquen, O. (2006). A constitutive law for dense granular flows. Nature, 441(7094), 727-730.
Moriguchi, S., Borja, R. I., Yashima, A., & Sawada, K. (2009). Estimating the impact force generated by granular flow on a rigid obstruction. Acta Geotechnica, 4(1), 57-71. https://doi.org/10.1007/s11440-009-0084-5
Ng, C. W. W., Jia, Z., Poudyal, S., Bhatta, A., & Liu, H. (2023). Two-phase MPM modelling of debris flow impact against dual rigid barriers. Géotechnique, 1-14. https://doi.org/10.1680/jgeot.22.00199
Ng, C. W. W., Wang, C., Choi, C. E., De Silva, W. A. R. K., & Poudyal, S. (2020). Effects of barrier deformability on load reduction and energy dissipation of granular flow impact. Computers and Geotechnics, 121. https://doi.org/10.1016/j.compgeo.2020.103445
Pastor, M., Haddad, B., Sorbino, G., Cuomo, S., & Drempetic, V. (2009). A depth-integrated, coupled SPH model for flow-like landslides and related phenomena. International Journal for Numerical and Analytical Methods in Geomechanics, 33(2), 143-172. https://doi.org/10.1002/nag.705
Peng, C., Guo, X., Wu, W., & Wang, Y. (2016). Unified modelling of granular media with Smoothed Particle Hydrodynamics. Acta Geotechnica, 11(6), 1231-1247. https://doi.org/10.1007/s11440-016-0496-y
Prime, N., Dufour, F., & Darve, F. (2014). Solid-fluid transition modelling in geomaterials and application to a mudflow interacting with an obstacle. International Journal for Numerical and Analytical Methods in Geomechanics, 38(13), 1341-1361. https://doi.org/10.1002/nag.2260
Redaelli, I., Ceccato, F., Di Prisco, C., & Simonini, P. (2017). Solid-fluid transition in granular flows: MPM simulations with a new constitutive approach. Procedia Engineering, 175, 80-85.
Redaelli, I., di Prisco, C., & Vescovi, D. (2015). A visco-elasto-plastic model for granular materials under simple shear conditions. International Journal for Numerical and Analytical Methods in Geomechanics, 40(1), 80-104. https://doi.org/10.1002/nag.2391
Roscoe, K. H., Schofield, A. N., & Wroth, C. P. (1958). On the yielding of soils. Géotechnique, 8, 22-53.
Savage, S. B. (1998). Analyses of slow high-concentration flows of granulars. Journal of Fluid Mechanics, 377, 1-26.
Schofield, A., & Wroth, C. (1968). Critical State Soil Mechanics. McGraw-Hill: London, U.K.
Si, P., Shi, H., & Yu, X. (2018). A general frictional-collisional model for dense granular flows. Landslides, 16(3), 485-496. https://doi.org/10.1007/s10346-018-1108-8
Song, D., Zhou, G. G. D., & Chen, Q. (2021). Flow resistance in the transition from dense to dilute granular-fluid flows. Granular Matter, 23(3). https://doi.org/10.1007/s10035-021-01134-1
Vescovi, D., di Prisco, C., & Berzi, D. (2013). From solid to granular gases: The steady state for granular materials. International Journal for Numerical and Analytical Methods in Geomechanics, 37(17), 2937-2951. https://doi.org/10.1002/nag.2169
Vescovi, D., Marveggio, P., & Di Prisco, C. G. (2020). Saturated granular flows: Constitutive modelling under steady simple shear conditions. Géotechnique, 70(7), 608-620. https://doi.org/10.1680/jgeot.19.P.023
Vicari, H., Tran, Q. A., Nordal, S., & Thakur, V. (2022). MPM modelling of debris flow entrainment and interaction with an upstream flexible barrier. Landslides, 19(9), 2101-2115. https://doi.org/10.1007/s10346-022-01886-8
Wang, B., Chen, P. L., Wang, D., Liu, L. L., & Zhang, W. (2023). Development of a GPU-

accelerated implicit material point method for geotechnical engineering. Acta Geotechnica. https://doi.org/10.1007/s11440-023-02155-1
Wang, Y., & Wu, W. (2024). Hypoplastic model for solid-like and fluid-like granular flows. Computers and Geotechnics, 172. https://doi.org/10.1016/j.compgeo.2024.106466
Wroth, C. (1958). Soil behaviour during shear—existence of critical void ratios. Engineering, 186, 409-413.
Yavari-Ramshe, S., Ataie-Ashtiani, B., & Sanders, B. F. (2015). A robust finite volume model to simulate granular flows. Computers and Geotechnics, 66, 96-112.
Yin, Z. Y., Hicher, P. Y., & Jin, Y. F. (2020). Practice of constitutive modelling for saturated soils. Springer Singapore.
Yin, Z. Y., Huang, H. W., & Hicher, P. Y. (2016). Elastoplastic modeling of sand-silt mixtures. Soils and Foundations, 56(3), 520-532. https://doi.org/10.1016/j.sandf.2016.04.017
Yin, Z. Y., Jin, Z., Kotronis, & Panagiotis, et al. (2018). Novel SPH simsand-based approach for modeling of granular collapse. International Journal of Geomechanics.
Yin, Z. Y., Xu, Q., & Hicher, P. Y. (2013). A simple critical-state-based double-yield-surface model for clay behavior under complex loading. Acta Geotechnica, 8(5), 509-523. https://doi.org/10.1007/s11440-017-0586-5
Yin, Z. Y., Zhao, J., & Hicher, P. Y. (2014). A micromechanics-based model for sand-silt mixtures. International Journal of Solids and Structures, 51(6), 1350-1363.
Zhang, Y., Zhang, X., Nguyen, H., Li, X., & Wang, L. (2023). An implicit 3D nodal integration based PFEM (N-PFEM) of natural temporal stability for dynamic analysis of granular flow and landslide problems. Computers and Geotechnics, 159, 105434.
Zheng, Q. J., & Yu, A. B. (2015a). Finite element investigation of the flow and stress patterns in conical hopper during discharge. Chemical Engineering Science, 129, 49-57.
Zheng, Q. J., & Yu, A. B. (2015b). Modelling the granular flow in a rotating drum by the Eulerian finite element method. Powder Technology, 286, 361-370.
Zhu, C., Wu, W., Peng, C., Wang, S., & Wei, X. (2024). SPH implementation of a critical state-based hypoplastic model for granular materials in large-deformation problems. Computers and Geotechnics, 166. https://doi.org/10.1016/j.compgeo.2023.106011
Savage, S. B., Sayed, M. (1984). Stresses developed by dry cohesionless granular materials sheared in an annular shear cell. Journal of Fluid Mechanics, 142, 391–430.
Cascini et al. (2016), Lee and Huang(2010), Si et al.(2018),Redaelli et al.(2017), Jop et al.(2006), Savage and Sayed (1984), Berzi et al. (2011), Vescovi et al. (2013)

Appendix A: Auxiliary functions in collisional stress

F, *J*, and *Q* are the auxiliary functions defined according to studies by (Garzo and Dufty, 1999; Berzi et al., 2014; Vescovi et al., 2013).

$$F = \frac{1}{4G} + \frac{1+\varepsilon_n}{2} \tag{A1}$$

$$J = \frac{25\pi(1+e)\eta^*}{768G} \tag{A2}$$

$$Q = \frac{5\pi(1+e)\gamma^*}{128G} \tag{A3}$$

where η^* and γ^* are expressed as:

$$\eta^* = \eta^{\kappa^*}\left[1+\frac{4}{5}G(1+\varepsilon_n)\right] + \frac{3}{5}\gamma^* \tag{A4}$$

$$\gamma^* = \frac{128}{5\pi}G(1+\varepsilon_n)\left(1-\frac{1}{32}c^*\right) \tag{A5}$$

$$\eta^{\kappa^*} = \left(\nu_\eta^* - \frac{1}{2}\zeta^{0^*}\right)^{-1}\left[1-\frac{2}{5}(1+\varepsilon_n)(1-3\varepsilon_n)G\right] \tag{A6}$$

$$\zeta^{0^*} = \frac{5}{12}g_0\left(1-\varepsilon_n^2\right)\left(1+\frac{3}{32}c^*\right) \tag{A7}$$

$$\nu_\eta^* = g_0\left[1-\frac{1}{4}(1-\varepsilon_n)^2\right]\left[1-\frac{1}{64}c^*\right] \tag{A8}$$

$$c^* = 32(1-e_n)\left(1-2e_n^2\right)\left[81-17e_n+30e_n^2(1-e_n)\right]^{-1} \tag{A9}$$

Appendix B: Fluctuating energy balance in collisional mechanism

The expression for the energy balance is derived according to (Vescovi et al., 2014), considering the energy conservation for the granular material, we have:

$$\rho \frac{D\mathcal{E}}{Dt} = \nabla \cdot (\mathbf{u} \cdot \sigma) - \nabla \cdot \mathbf{q} - \Gamma_E \tag{B1}$$

where $\mathcal{E}$ is the internal specific energy per unit mass; $\nabla \cdot (\mathbf{u} \cdot \sigma)$ is the work by the stress; $\mathbf{q}$ is the flux of energy; Γ_E is the rate of energy dissipation.

The internal energy $\mathcal{E}$ can be decomposed into two parts:

$$\mathcal{E} = \mathcal{E}_h + \mathcal{E}_k \tag{B2}$$

where $\mathcal{E}_h$ is the specific true thermal energy of the material, it can be ignored considering that it is ten orders of magnitude less than the specific kinetic energy $\mathcal{E}_k$. The specific kinetic energy $\mathcal{E}_k$, can be decomposed into two contributions: the mean kinetic energy $\mathcal{E}_{k,m}$ and fluctuating kinetic energy $\mathcal{E}_{k,f}$. Accordingly, Eq.(B1) can be rewritten as:

$$\rho \frac{D\left(\mathcal{E}_{k,m} + \mathcal{E}_{k,f}\right)}{Dt} = \nabla \cdot (\mathbf{u} \cdot \boldsymbol{\sigma}) - \nabla \cdot \mathbf{q} - \Gamma_E \tag{B3}$$

Eq.(B3) can be further reduced into:

$$\rho \frac{D\mathcal{E}_{k,m}}{Dt} = \mathbf{u} \cdot \nabla \cdot \boldsymbol{\sigma} \tag{B4}$$

$$\rho \frac{D\mathcal{E}_{k,f}}{Dt} = \boldsymbol{\sigma} \cdot \nabla \cdot \mathbf{u} - \nabla \cdot \mathbf{q} - \Gamma_E \tag{B5}$$

Based on the parallel scheme, we have $\boldsymbol{\sigma} = \boldsymbol{\sigma}_f + \boldsymbol{\sigma}_{col}$, $\mathbf{q} = \mathbf{q}_f + \mathbf{q}_{col}$, and $\Gamma_E = \Gamma_f + \Gamma_{col}$. Substituting these equations into Eq. (B5), and we suppose the $0 = \boldsymbol{\sigma}_f \cdot \nabla \cdot \mathbf{u} - \nabla \cdot \mathbf{q}_f - \Gamma_f$. Hence, the balance of fluctuating kinetic energy can be rewritten as:

1027 $$\rho \frac{D\mathcal{E}_{k,f}}{Dt} = \boldsymbol{\sigma}_{col} \cdot \nabla \cdot \mathbf{u} - \nabla \cdot \mathbf{q}_{col} - \Gamma_{col} \tag{B6}$$

1028 The kinetic fluctuating energy can be expressed using the granular temperature $\mathcal{E}_{k,f} = \frac{3}{2}T$.

1029 The symmetric characteristics $\nabla \cdot \mathbf{u}$ can be expressed using $\nabla \cdot \mathbf{u} = \dot{\boldsymbol{\varepsilon}}$. Then, Eq.(B6) is derived into:

1030 $$\boldsymbol{\sigma}_{\mathrm{col}} : \dot{\boldsymbol{\varepsilon}} = \frac{3}{2}\frac{\rho_p}{1+e}\dot{T} + \nabla \cdot \mathbf{q}_{col} + \Gamma_{col} \tag{B7}$$

1031 where Γ_{col} is the rate of energy dissipation by the collisional mechanism, expressed as:

1032 $$\Gamma_{col} = \frac{144}{5\sqrt{\pi}}\frac{\rho_p}{d}\frac{T^{3/2}\zeta^*}{(1+e)} \tag{B8}$$

1033 where ζ^* is expressed as:

1034 $$\zeta^* = \zeta^{0*} + \zeta^{1*} \tag{B9}$$

1035 $$\zeta^{0*} = \frac{5}{12}g_0\left(1-\varepsilon_n^2\right)\left(1+\frac{3}{32}c^*\right) \tag{B10}$$

1036 $$\zeta^{1*} = \left[-\frac{5}{96}\frac{d(1+e)}{1}\sqrt{\frac{\pi}{T}}(1-\varepsilon_n)(p^*-1) + \frac{5}{32}\left(1-\varepsilon_n^2\right)\left(1+\frac{3}{64}c^*\right)g_0 C_d\right]\nabla \cdot \mathbf{u} \tag{B11}$$

1037 where C_d is expressed as:

1038
$$C_d = \frac{5d(1+e)}{96}\sqrt{\frac{\pi}{T}}\frac{\frac{4}{15(1+e)}\lambda g_0 + (p^*-1)\left(\frac{2}{3}-e_n\right)c^*}{\frac{1}{2}\zeta^{0*} + \nu_\gamma^* + \frac{5}{64}c^*\left(1+\frac{3}{64}c^*\right)g_0\left(1-\varepsilon_n^2\right)} \quad \text{(B12)}$$

1039
$$\nu_\gamma^* = \frac{1+\varepsilon_n}{48}g_0\left[128-96\varepsilon_n+15\varepsilon_n^2-15\varepsilon_n^3+\frac{c^*}{64}(15\varepsilon_n^3-15\varepsilon_n^2+498\varepsilon_n-434)\right] \quad \text{(B13)}$$

1040
$$\lambda = \frac{3}{8}\left[(1-\varepsilon_n)\left(5\varepsilon_n^2+4\varepsilon_n-1\right)+\frac{c^*}{12}\left(159\varepsilon_n+3\varepsilon_n^2-19\varepsilon_n-15\varepsilon_n^3\right)\right] \quad \text{(B14)}$$

1041

Appendix C: Mesh sensitivity analysis

A mesh sensitivity analysis is carried out to choose a rational mesh approach in section. Because increasing the number of material points in a coarse mesh does not significantly improve the mesh quality (Fern and Soga, 2016), the variable mesh size is considered. Table. C-1 has listed the different cases in column collapse, in which the grid size is changed from 0.01 to 0.001. The results of these cases are shown in Fig. C-1. It is clear that decreasing the grid size can significantly improve the mesh quality. Considering the calculation and mesh quality, C-4 with a grid size of 0.001 m is chosen for the simulation.

Table C-1. MPM model setup information of the column collapse

Colum collapse	Grid size (m)	MPs/cell	MPs	Time (min)
C-1	0.01	4	200	1.24
C-2	0.005	4	3200	6.78
C-3	0.0025	4	12800	100.1
C-4[a]	0.001	4	80000	240.53

[a] default case

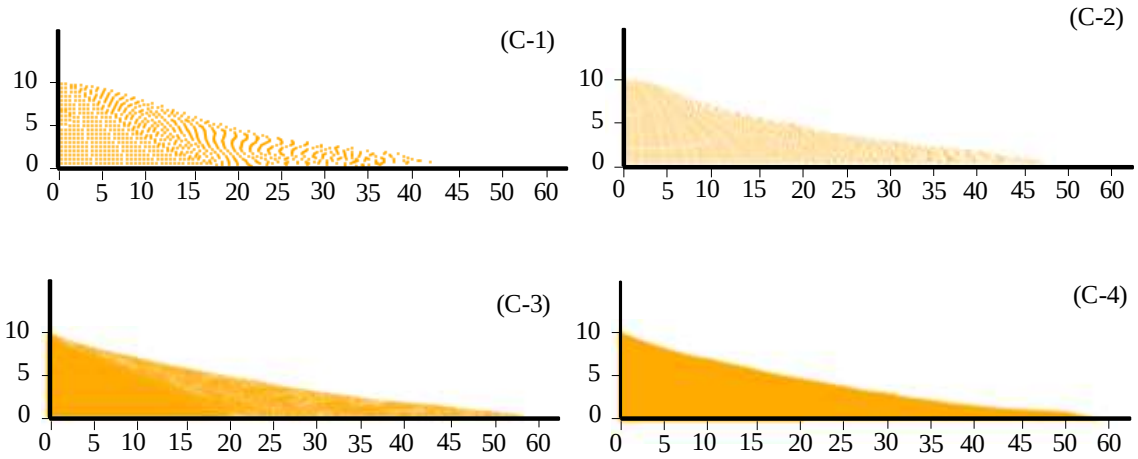

Fig. C-1. Comparison of free surface configurations in sand column collapse for different mesh sizes.

Table. C-2 has listed the different cases in slump test, in which the grid size is changed from 0.02 to 0.0025. The results of these cases are shown in Fig. C-2. Considering the calculation and mesh quality, S-4 with a grid size of 0.005 m is chosen for the simulation.

Table C-2. MPM model setup information of the slump test

Slump test	Grid size (m)	MPs/cell	MPs	Time (min)
S-1	0.02	4	1500	4.24
S-2	0.01	4	6000	8.67
S-3[a]	0.005	4	24000	240.01
S-4	0.0025	4	96000	450.53

[a] default case

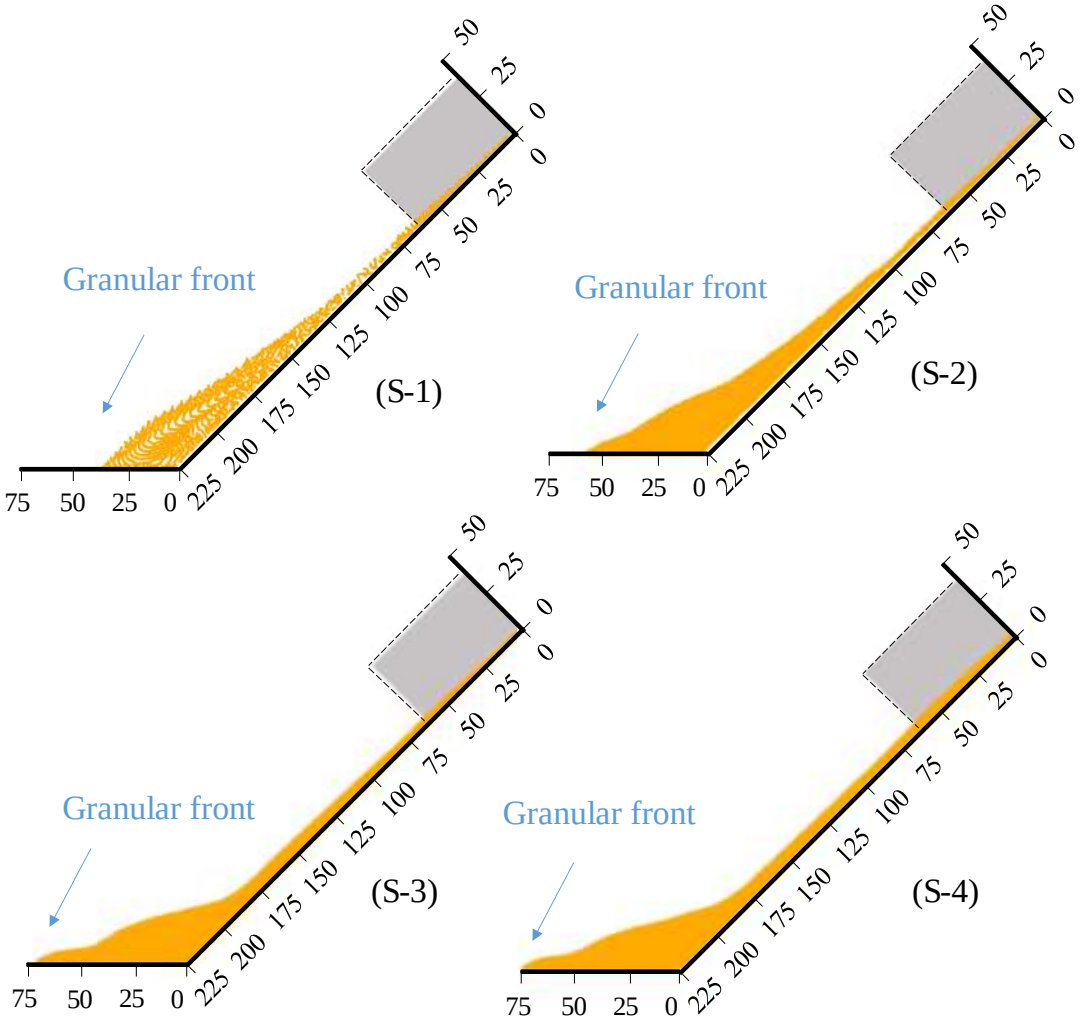

Fig. C-2. Comparison of free surface configurations in flume test for different mesh sizes